Characterization of surface wetting uniformity in hydrophobic tubes using ferrofluid droplets

Vivien Lefranc

School of Science

Thesis submitted for examination for the degree of Master of Science in Technology.

Espoo 20.8.2019

Supervisor

Prof. Robin Ras

Advisor

MSc Mika Latikka

Aalto University
School of Science

Aalto University
School of Science

Aalto University, P.O. BOX 11000, 00076 AALTO
www.aalto.fi
Abstract of the master's thesis

Author Vivien Lefranc

Title Characterization of surface wetting uniformity in hydrophobic tubes using ferrofluid droplets

Degree programme Advanced Materials for Innovation and Sustainability

Major Advanced Materials for Innovation and Sustainability **Code of major** SCI3083

Supervisor Prof. Robin Ras

Advisor MSc Mika Latikka

Date 20.8.2019 **Number of pages** 50+1 **Language** English

Abstract

Hydrophobic surfaces, or water repellent surfaces, have interesting properties for applications on self-cleaning, anti-icing, antifogging and fluid drag reduction. To develop more efficient surfaces, proper characterization methods need to be developed as the current methods available are not sufficient. In this thesis, the theoretical background behind wetting phenomena on hydrophobic surfaces and various techniques for characterizing wetting properties are presented. Furthermore, a new characterization technique applied to hollow, non planar surfaces and more specifically to transparent tubes is proposed. This technique measures wetting inhomogeneities using magnetically controlled water-like droplets over the entire length of the samples. This technique can measure the retentive force, a dissipative force related to the contact angle hysteresis at the three-phase contact line. This technique is used to see differences in wetting properties using reference tubes and their annealed counterparts using two different ferrofluids. As a non-destructive and quantitative characterization method, this technique could readily be used for quality control in academia and industries.

Keywords Ferrofluid, wetting properties, hydrophobicity, superparamagnetic nanoparticles

Preface

Experimental work presented in this thesis was conducted in the Soft Matter and Wetting group, at the Department of Applied Physics in Aalto University School of Science in 2019.

First of all, I would like to thank my advisor Mika Latikka which helped and guided through this project. I learned a lot during this thesis and it is thanks to him for the most part.

I would also like to thank my supervisor Professor Robin Ras for welcoming me in his group and allowing me to work on this very interesting topic.

I want to thank my colleagues of the Soft Matter and Wetting group and of the Department of Applied Physics for making me feel like a proper member of their research team.

Finally, I would like to thank my friend Monish Rajkumar for his encouragements during the writing of this thesis.

Espoo, August 20, 2019

Vivien Lefranc

Contents

Operators and abbreviations

Operators

$\frac{\mathrm{d}}{\mathrm{d}t}$	derivative with respect to variable t
$\frac{\partial}{\partial t}$	partial derivative with respect to variable t
$\sum_{i=1}^{n}$	sum over index i from 1 to n

Abbreviations

ACA	Advancing Contact Angle
CA	Contact Angle
CAH	Contact Angle Hysteresis
CL	Contact Line
ODT	Oscillating Droplet Tribometer
PBS	Phosphate-Buffered Saline
RCA	Receding Contact Angle
RRF	Reduced Retentive Force
SDAM	Scanning Droplet Adhesion Microscopy

List of Figures

List of Tables

1 Introduction

Hydrophobic, or water repellent, surfaces have a wide range of applications. Be it in the fields of self-cleaning [1]–[4], anti-icing [5]–[10], antifogging [11], directional transportation [12], [13], fluid drag reduction [14], [15], water collection [16]–[18] or non-wetting textiles [19]. Hydrophobic surfaces are defined by micro- or nanoscale surface roughness as well as low surface energy [20]. This leads to a decreased area of contact between water and the surface as the water lies mostly on an air layer formed in the topography of the material [21]. As a result, the adhesion between water and the surface decreases, thus ensuing high droplet mobility and reduced drag in liquid flow [21]–[25]. Although water repellency has been observed in nature for thousands of years, the physical behavior behind superhydrophobic surface, or extremely water repellent surfaces was only investigated in 1997 by W. Barthlott and C. Neinhuis using sacred lotus leaves [4]. Since then, interest on the topic of hydrophobic and superhydrophobic surfaces has considerably grown.

Intensive research is underway on different processes and materials to make such surfaces. Current research focuses on easily applied hydrophobic coatings, and hydrophobic surfaces with durable topography [26]. With them, a number of characterization techniques were adapted from historic methods and perfected. For example, hydrophobic surfaces are commonly investigated using contact angle goniometry which is much older than any artificially made superhydrophobic surface. The techniques used are relatively fast and accurate for hydrophobic surfaces but they are poorly fit for superhydrophobic surfaces considering the optical errors the methods imply. New techniques are being developed in order to have more precise measurements, even allowing a direct mapping of wetting properties of a surface[27], [28]. But these are still limited to simple planar surfaces. There is thus a need for newer characterization methods applicable to more complex geometries other than planar surfaces, such as conical tubes. To the author's knowledge, there is no method available for measuring inhomogeneities in wetting properties in such geometry for hydrophobic samples.

In this paper, we will propose a new characterization technique applied to hollow, non planar surfaces and more specifically to transparent hydrophobic tubes. The first part of this thesis introduces the principles behind hydrophobicity and highlights different characterization techniques with their strengths and weaknesses. In the second part of this paper, a new characterization technique applied to transparent hydrophobic tubes is proposed. This method measures wetting inhomogeneities using magnetically controlled water-like droplets other the whole length of the samples. It can measure the retentive force, a dissipative force related to the contact angle hysteresis at the three-phase contact line. As a non-destructive and quantitative characterization method, this technique could readily be used for quality control in academia and industries.

2 Theory

Water is present in all state of life on earth. A natural consequence of evolution is the adaption of living plants or animal species to water. Indeed, living beings developed very ingenious ways of interacting with liquids through hydrophobicity. From water striders that can "walk on water", making use of the high surface tension of water [29], to the "lotus effect" which protect lotus leaves from fungus and prevent dirt from forming on top of it[4], the examples are numerous. As such, hydrophobicity has been known for a long time, especially in Asian cultures, and mentions of the lotus effect were made in various sacred scriptures like the Hindu text Bhagavad Gita [30]. However, the first relevant scientific approach to explain wetting phenomena was conducted in 1805 by Thomas Young.

2.1 Contact Angles

2.1.1 Young Contact Angle

In his "*Essay on the cohesion of fluids*"[31], Young describes the existence of a unique contact angle (CA) between the solid-liquid interface and the liquid-air interface for each specific three-phases system. He also anticipates that the CA is dependant of the cohesive forces between each phases and inside the liquid phase itself. The contact angle is represented in figure 1.

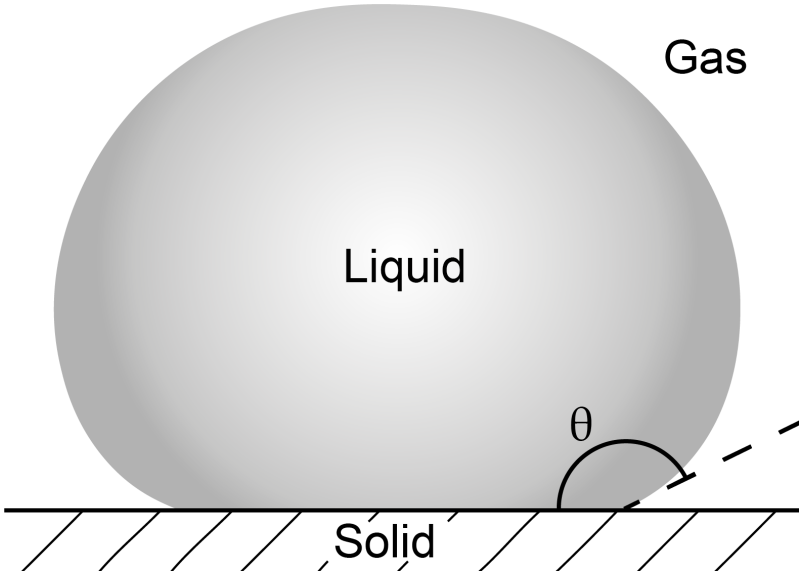

Figure 1: Schematic of a droplet of liquid on a solid surface. The angle θ represent the contact angle between the solid-liquid interface and the liquid-gas interface.

The CA, more than just a simple angle, has a *physical* signification. The higher it is, the more water-repellent the surface will be. It is thus the main indicator for wetting properties. The CA is related to interfacial tensions between the different phases. In a phase, molecules present on the surface have higher energy than molecules

in the bulk. It is due to the lack of neighbour molecules at the surface, thus, the molecules at the surface are attracted toward the bulk. As such, the internal pressure is increased for liquids and the surface minimizes as the droplet will be more stable at lower energy values. By definition, the work needed to increase the surface area is often assimilated to the interfacial tension of the surface, or surface tension.

Mathematically, the interfacial tension can be defined as the increase in Gibbs free energy G of the system when the surface area of liquid A is increased while the temperature T, the volume V and the number of molecules in the system n are constant:

$$\gamma = \left[\frac{\partial G}{\partial A}\right]_{(T,V,n)} \tag{1}$$

Thus, interfacial tension γ is interpreted as surface energy per unit area. Similarly, interfacial tension can be defined with the work required to increase the surface area:

$$\delta W = \gamma dA \tag{2}$$

If we consider a perfectly flat surface, when a droplet of water is deposited on a solid, a solid-liquid interface is created and the same area of solid-gas and liquid-gas is destroyed. Since the total work is equal to the sum of all the different works, it leads to this equation :

$$\delta W = \delta W_{sg} + \delta W_{sl} + \delta W_{lg} \tag{3}$$

Where :

$$\delta W_{sg} = -\gamma_{sg} dA; \delta W_{sl} = \gamma_{sl} dA; \delta W_{lg} = -\gamma_{lg} dA \tag{4}$$

And :

$$\frac{\delta W}{dA} = -(\gamma_{sg} + \gamma_{lg}) + \gamma_{sl} \tag{5}$$

The work of adhesion W_A can be defined as the work needed to separate two adjacent phases from each other. This work of adhesion is an energy per unit area and is related to the previous work calculated by :

$$W_A = -\frac{\delta W}{dA} \tag{6}$$

Thus :

$$W_A = \gamma_{sg} + \gamma_{lg} - \gamma_{sl} \tag{7}$$

According to Young, "*for each combination of a solid and a fluid, there is an appropriate angle of contact between the surfaces of the fluid, exposed to the air, and to the solid.*" [31]. It means that a unique contact angle exists for a specific solid surface, liquid droplet and gas phase system at equilibrium. Young's contact angle equation gives a relation between the surface tensions and the CA. It is given by the following :

$$cos(\theta_Y) = \frac{\gamma_{sg} - \gamma_{sl}}{\gamma_{lg}} \tag{8}$$

Whereθ_Y is the Young contact angle, γ_{sg} is the surface tension (energy per unit surface) of the solid–vapor interface, γ_{sl} is the surface tension of the solid–liquid interface and γ_{lg} is the surface tension of the liquid-vapor interface. This equation is valid in case of force equilibrium at the three-phase contact line (CL). On combining equations 7 and 8, we obtain :

$$W_A = \gamma_{lg}(1 + cos\theta_Y) \tag{9}$$

It shows, with equation 8, that the contact angle is dependant on the surface energy of the solid, and since in hydrophobicity we mostly investigate water as a liquid and ambient air as the gas, γ_{lg} is a constant at constant temperature for an ideal surface. But Young equation depends on a few hypotheses : evaporation is negligible and the substrate is an ideal surface. An ideal surface is chemically homogeneous, atomically smooth, nondeformable by the liquid and does not interact chemically with the liquid [32]. The wetting system examined in this section is thus a highly idealized one, and equation 8 is even a further simplification of such a system. The equation also assumes that the interactions at the CL are strictly pair-wise, which is not always the case. The interactions between the three phases can be taken into account by introducing a new term called line tension. However, the line tension is significant only for droplets with CL radius shorter than few micrometers [33]. It is not the case for our system since we use droplets of the μL order of magnitude. As such, the effects of line tension are not considered further in this thesis.

Table 1: Scale of hydrophilicity, hydrophobicity and superhydrophobicity from 0 to 180 degrees with schematic on top of scale.

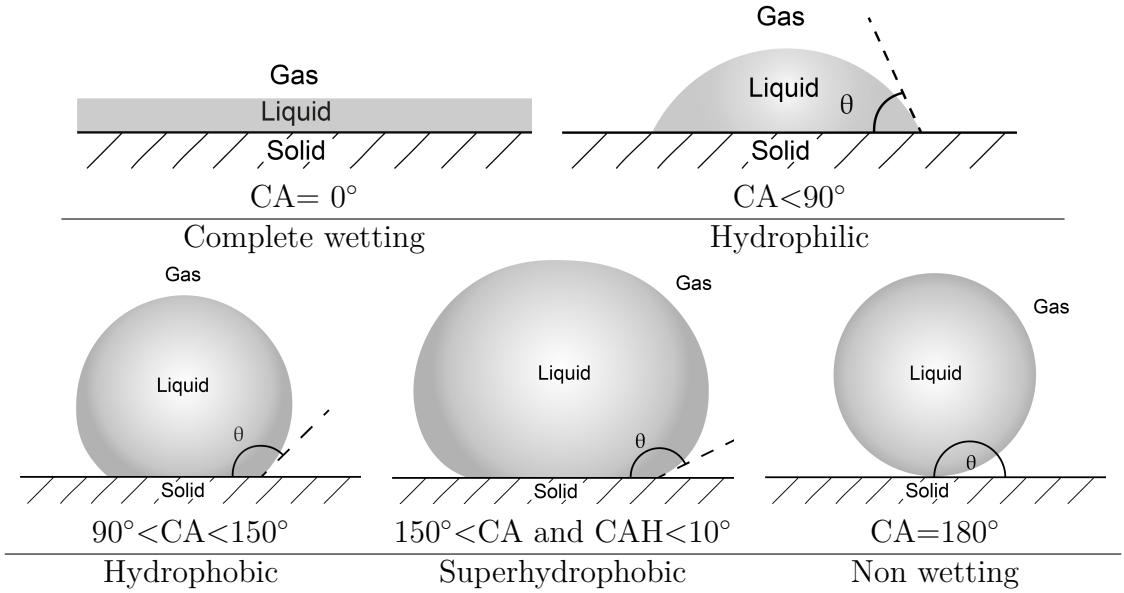

In the table 1, we define the different wetting behaviors related to CAs. The CA can range from 0° to 180°, from hydrophilic to superhydrophobic surfaces.

2.1.2 Apparent Contact Angle

In reality, surfaces are never perfect and are usually heterogeneous. The Young CA is changing all along the surface due to this heterogeneity. However, most inhomogeneities are smaller than typical droplet size, making the local CA very hard to observe. Microscopic or nanoscopic surface roughness also adds more difficulties to access a precise value of the Young CA. A distinction is thus made between the apparent CA and the Young CA for rough surfaces as shown in figure 2 due to roughness.

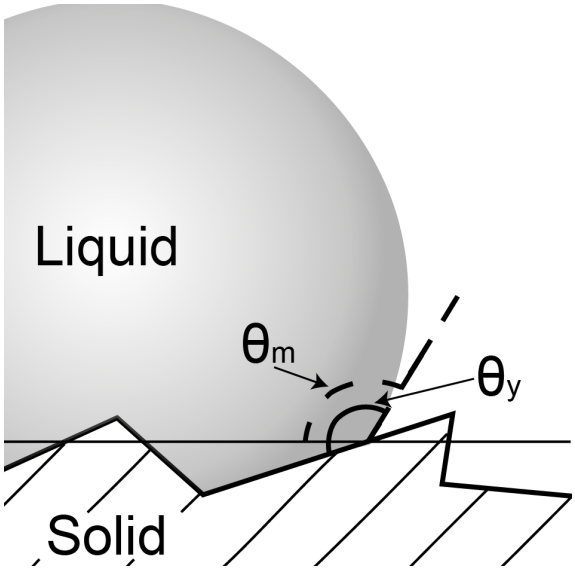

Figure 2: Magnification of the apparent three-phase contact line on a rough surface. The measured contact angle θ_m is different from the real contact angle θ_y due to the roughness.

Near the CL, at the microscopic scale, Young's equation (8) determine the shape of the liquid-gas interface. However, as shown in figure 2, the CA measured is different from the Young CA. The macroscopic shape of the droplet is defined by the difference in capillary pressure across the liquid-gas interface. It follows the Young-Laplace equation [31]:

$$\Delta p = \gamma_{lg} \left(\frac{1}{R_1} + \frac{1}{R_2} \right) \tag{10}$$

Where R_1 and R_2 are the radii of curvature and Δp the pressure difference between the inside and the outside of the droplet. Current CA analysis softwares determine the shape of the droplet excluding the curvature near the CL position and fit the results with this equation in order to extrapolate the droplet shape at the CL. It leads to a more rigorous result as the fit will only take into account the materials properties and avoid errors related to magnification at the CL. As such, the apparent CA is easily attained compared to the Young CA which gives information on the interfacial tensions but is in practice hard to measure. That is why if there is no other mention, "CA" will now refer to apparent CA in this thesis.

2.2 Wetting Models

The definitions given in the previous section sets the foundation of the wetting theory but are not enough for complex systems such as hydrophobic surfaces. In this section, two major models on wetting phenomena will be introduced : the Wenzel model (1936) and the Cassie-Baxter model (1944).

2.2.1 Wenzel Model

Wenzel studied the wetting properties of waterproof open fabrics and of water-repelling agents in his paper on the "Resistance of solid surfaces to wetting by water" [34]. The Wenzel model considers a rough and chemically homogeneous surface. According to the author, wettability depends not only on surface tensions, but also on the physical condition of the surface. The solid-liquid interface is of paramount importance and roughness changes the area of contact of the liquid on the surface. This rough area is the *real* area A_{real} and takes into account the micro-roughness, as opposed to the *geometric* area $A_{geometric}$ which appears flat and is the vertical projection of the real area. The ratio between the two $r = \frac{A_{real}}{A_{geometric}}$ is called the roughness factor. The roughness leads to a greater intensity of surface energy than in the same measured unit area for a smooth surface but does not change the liquid-air interfacial energy. Therefore, a rough surface is more water-repellent and its CA increases for a hydrophobic material. This roughness effect is represented in figure 3.

A relation between the CA of a smooth surface, θ, and the CA of a rough surface, θ', can be described. The adhesion force related to the surface for a flat surface is $A = F_{sl} - F_{sg}$ with F_{sl} and F_{sg} the forces related to the solid-liquid and the solid-gas interfaces respectively. The force applied by the liquid-gas interface is F_{lg}. In case of a smooth and of a rough surface, the force equilibrium gives (in the following A and F_{lg} are the intensity of the forces $\mathbf{A}$ and F_{lg}):

$$A = F_{lg}cos(\theta) \tag{11}$$

And

$$rA = F_{lg}cos(\theta') \tag{12}$$

By combining equations 11 and 12, we obtain :

$$rcos(\theta) = cos(\theta') \tag{13}$$

When combining this equation with Young equation (8), the *Wenzel* equation on the effects of roughness on surface wetting properties is obtained:

$$cos(\theta_W) = rcos(\theta_Y) = r\frac{\gamma_{sg} - \gamma_{sl}}{\gamma_{lg}} \tag{14}$$

Where θ_W is the previous θ' and θ_Y is the previous θ. Wenzel equation is of general validity: for smooth surfaces, $r = 1$ and $\theta_W = \theta_Y$. It also predicts an increase in both hydrophobic and hydrophilic effects. Indeed, if $\theta_Y < 90°$, then $\theta_W < \theta_Y$ and if $\theta_Y > 90°$, $\theta_W > \theta_Y$.

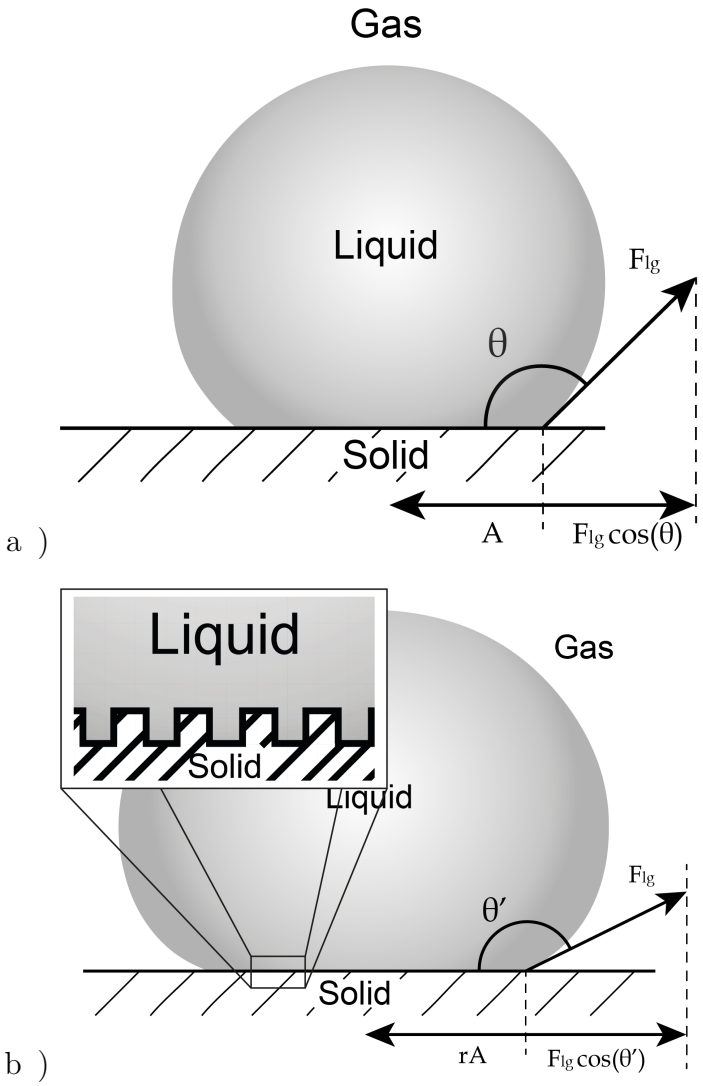

Figure 3: Droplet on a) a smooth surface and b) a rough surface with a roughness factor r=2. **A** is the adhesion force related to the surface for a flat surface: $A = F_{sl} - F_{sg}$ with F_{sl} and F_{sg} being the forces related to the solid-liquid and the solid-gas interfaces respectively. The adhesion force related to the surface for a rough surface is given by $r\boldsymbol{A}$ and is larger due to the increased surface area. The adhesion force is balanced by the force applied by the liquid-gas interface F_{lg} whose intensity does not vary. Thus, the CA is increased from θ to θ' for a rough surface in order to balance the projected F_{lg} and rA.

With increasing roughness, a hydrophilic surface becomes more hydrophilic and a hydrophobic surface more hydrophobic. However, this model is only valid if the liquid wets the cavities entirely. It is hardly the case when the surface is highly hydrophobic (and thus the surface energy of wet surface is higher than the surface energy of dry surface) which repulse water. Furthermore, with increased roughness, water resting on top of surface topography becomes more energetically favorable and

air is bound to be trapped underneath the droplet. This effect is discussed in the next section on the Cassie-Baxter model.

2.2.2 Cassie-Baxter Model

Before looking at rough surfaces, the case of heterogeneous flat surfaces should be addressed first. We consider one surface with two phases of fractional areas σ_1 and σ_2 ($\sigma_1 + \sigma_2 = 1$). On this surface, the work required for a droplet of water to spread on a surface of total area A is :

$$W_S = (\sigma_1(\gamma_{s_1l} - \gamma_{s_1g}) + \sigma_2(\gamma_{s_2l} - \gamma_{s_2g}))A \tag{15}$$

γ_{s_1l} and γ_{s_2l} are the solid1-liquid and solid2-liquid surface tensions, γ_{s_1g} and γ_{s_2g} are the solid1-gas solid2-gas surface tensions. This expression is valid when $\sigma_1 A$ area of solid1-gas is replaced by the same area of solid1-liquid and likewise for solid phase 2. If equations 6 and 9 are combined while removing the part linked to the destruction of the liquid-gas interface which does not happen in the present system, we obtain :

$$-\frac{1}{\gamma_{lg}}\frac{W_S}{dA} = cos(\theta_Y) \tag{16}$$

Thus :

$$cos(\theta_c) = \sigma_1\frac{\gamma_{s1g} - \gamma_{s1l}}{\gamma_{lg}} + \sigma_2\frac{\gamma_{s2g} - \gamma_{s2l}}{\gamma_{lg}} \tag{17}$$

Young equation is applied to both solid phase 1 and 2 to finally obtain :

$$cos(\theta_c) = \sigma_1 cos(\theta_{Y1}) + \sigma_2 cos(\theta_{Y2}) \tag{18}$$

Which is the called the *Cassie* equation. The Cassie equation can also be generalized for a system with n number of phases :

$$cos(\theta_c) = \sum_{i=1}^{n} \sigma_i cos(\theta_{Yi}) \tag{19}$$

With $\sum_{i=1}^{n} \sigma_i = 1$. The CA given by the Cassie equation is an apparent CA and not a local CA.

Now, a rough heterogeneous hydrophobic surface is considered. Air bubbles will spontaneously form in the surface topography under the droplet thanks to the surface high energy. This air layer is called the *plastron*. Thus, the droplet is partly supported by the plastron and the peaks of the solid surface [35]. It is called the *Cassie-Baxter* state or the *fakir* state [36] due to the resemblance between such droplets and fakirs on top of a bed of nails as shown in figure 4.

We call f_{sl} and f_{lg} the area fractions of solid-liquid and liquid-gas interface in a rough surface under a droplet of water. As such, the Cassie equation can be applied to this system, with the second phase being the air, and this equation is obtained :

$$cos(\theta_{CB}) = r f_{sl} cos(\theta_{Y_{solid}}) + f_{lg} cos(\theta_{Y\,air}) \tag{20}$$

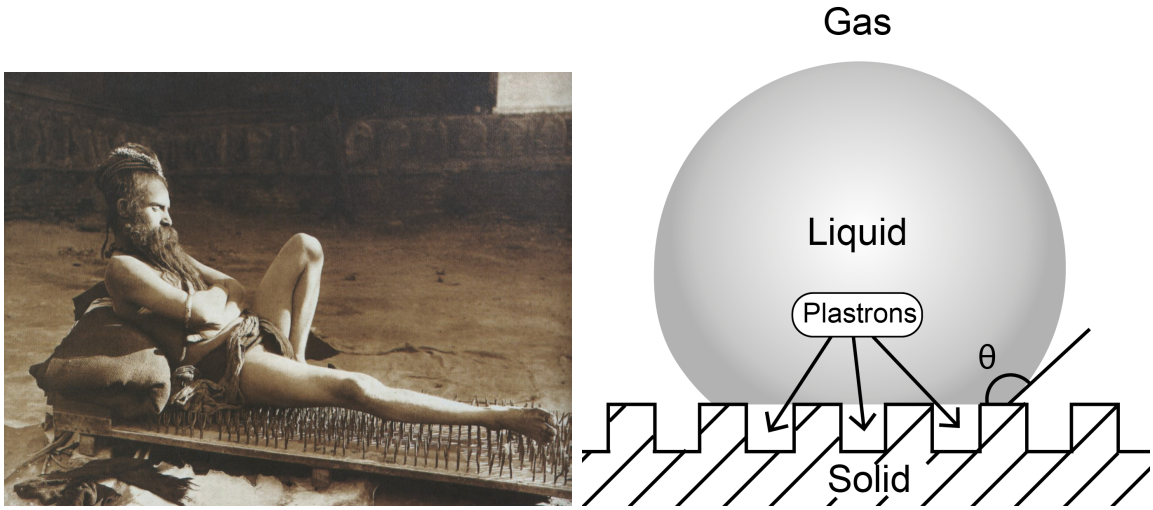

Figure 4: Analogy between a fakir on top of a bed of nails (taken from [37]) and a droplet in the Cassie-Baxter state. The fakir rests only on the tip of the nails and is not hurt because his weight is divided other numerous nails. For the droplet, it reposes both on the tip of the surface and the plastron due to the surface tension of water.

Since the Young CA of air is 180° (can be proved if the solid is replaced by the gas phase in young's equation), then $cos(\theta_{Y\,air}) = -1$ and then :

$$cos(\theta_{CB}) = r f_{sl} cos(\theta_Y) - f_{lg} \tag{21}$$

Here, θ_{CB} is the apparent CA. This equation is called the *Cassie-Baxter* equation [38]. It has the be noted that if f_{lg} =0, then $f_{sl} = 1$ and the Wenzel state is achieved. Thus, the equation reduces to Wenzel equation 14.

2.2.3 Comparison between Wenzel and Cassie-Baxter States

Energy comparison between the two models will be made in this section. In the Wenzel state, the surface energy per unit areq can be deducted from equation 7 when taking into account the roughness with the roughness factor r :

$$W_{A_W} = r(\gamma_{sg} + \gamma_{lg} - \gamma_{sl}) \tag{22}$$

$$W_{A_{CB}} = r f_{sl}(\gamma_{sg} + \gamma_{lg} - \gamma_{sl}) \tag{23}$$

As such, since $f_{sl} \leq 1$, then $W_{A_{CB}} \leq W_{A_W}$ in every situation. Also, the two surface energies can be multiple orders of magnitude apart when $f_{sl} \to 0$. Cassie-Baxter state is a requisite for superhydrophobic effects, because even the most hydrophobic materials, such as PTFE (poly(tetrafluoroethylene) i.e. Teflon), have relatively low CAs. The highest possible θ_Y on a homogeneous surface is 119°, achieved by hexagonally close-packed -CF3 [39]. Though Wenzel state also achieves high CAs, the adhesion of liquid to the solid surface is much higher due to large solid-liquid interface as seen by the previous comparison.

2.3 Contact Angle Hysteresis

These two previous models raise an important question, if a droplet reposes on a gradient of roughness or heterogeneity, will the droplet have a unique CA like Young suggested? The answer is no: there is not only one apparent CA for a given surface. If a sessile drop is in the Wenzel state or the Cassie-Baxter state then their CAs would be different. In reality there are numerous observable CAs for one droplet position. Indeed, if we consider everyday life, if there was only one stable contact angle as according to Young's equation, then the slightest tilt of a solid surface with a droplet on top of it would result in the droplet moving. Looking at sticky raindrops on car windshields can persuade the reader of this fact. First of all, roughness and chemical inhomogeneities can lead to the CL being pinned in certain ways. It leads to a multitude of metastable CAs. Secondly, from an energy perspective, the Gibbs energy curve is very complex due to opposing interactions driven by the interfacial tensions at the local CA scale as in Young equation 8 and the macroscopic shape of the droplet driven by the difference in pressure as in Young-Laplace equation 10. Thus, for a given solid-liquid-gas system, there is always a discrete range of apparent CAs visible and these CAs are local minima in the Gibbs energy curve as a function of apparent CA. A simplified energy curve is plotted in figure 5.

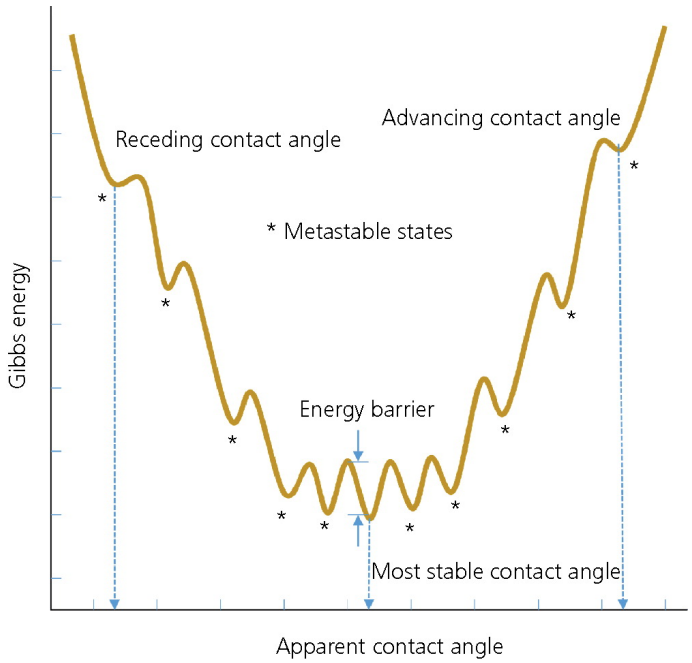

Figure 5: The Gibbs energy for a liquid on a rough or heterogeneous solid surface in function of the apparent CA, adapted from [32].

The minimal measurable metastable CA is called the Receding Contact Angle (RCA) and the maximum is the Advancing Contact Angle (ACA). The CA with the state of the lowest Gibbs energy is also called the most stable contact angle. A very important value is the Contact Angle Hysteresis (CAH) which is defined by the difference between the ACA and the RCA [32]. It is connected with the multiple

equilibrium positions of the drop edge on a rough surface. The higher the CAH is, the higher the pinning force induced on the droplet is. To characterize a surface, the ACA and the RCA are the values measured, as the most stable contact angle cannot be measured by commercially available goniometers [40].

In a static case, the CA value of a "just deposited" droplet on a substrate is in the interval between the RCA and the ACA. The dependency of the contact angle to the velocity of the advancing and receding meniscus of the droplet is represented in figure 6. In order to measure the RCA and the ACA, the CL must come to the point of moving. The ACA is the first CA attained when the velocity of the advancing meniscus is positive. Inversely, the RCA is the first CA attained when the velocity of the receding meniscus is negative [41]. This difference in CA between the advancing and receding meniscus lead to a force opposing the movement called the CAH-force. It will be introduced later in this work. Different characterization methods are available in order to measure the ACA and RCA, as well as newer techniques based on forces instead of CAs. They will be introduced briefly in the next section.

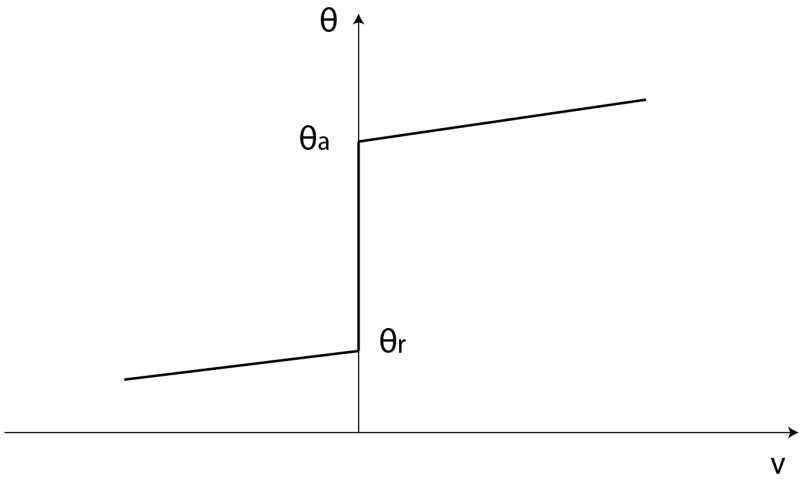

Figure 6: Dependency of the contact angle on the velocity of advancing (v>0) and receding (v<0) meniscus.

2.4 Characterization Methods

Using proper characterization techniques, researchers and industries are trying to make efficient hydrophobic surfaces in a reproducible way. Developing new characterization methods is of paramount importance to deepen our understanding of wetting phenomena, as new information can be gathered with those. Commonly used techniques will now be introduced, as well as newer techniques from which this current work stems from.

2.4.1 Contact Angle Goniometer Techniques

The contact angle goniometer allows a direct measurement of the contact angle of a droplet on top of a substrate by using a camera and an imaging software. There are two main methods : the sessile drop technique and the tilting plate method. They both allow a measure of the ACA and the RCA which are the only two reproducible CAs easily measurable.

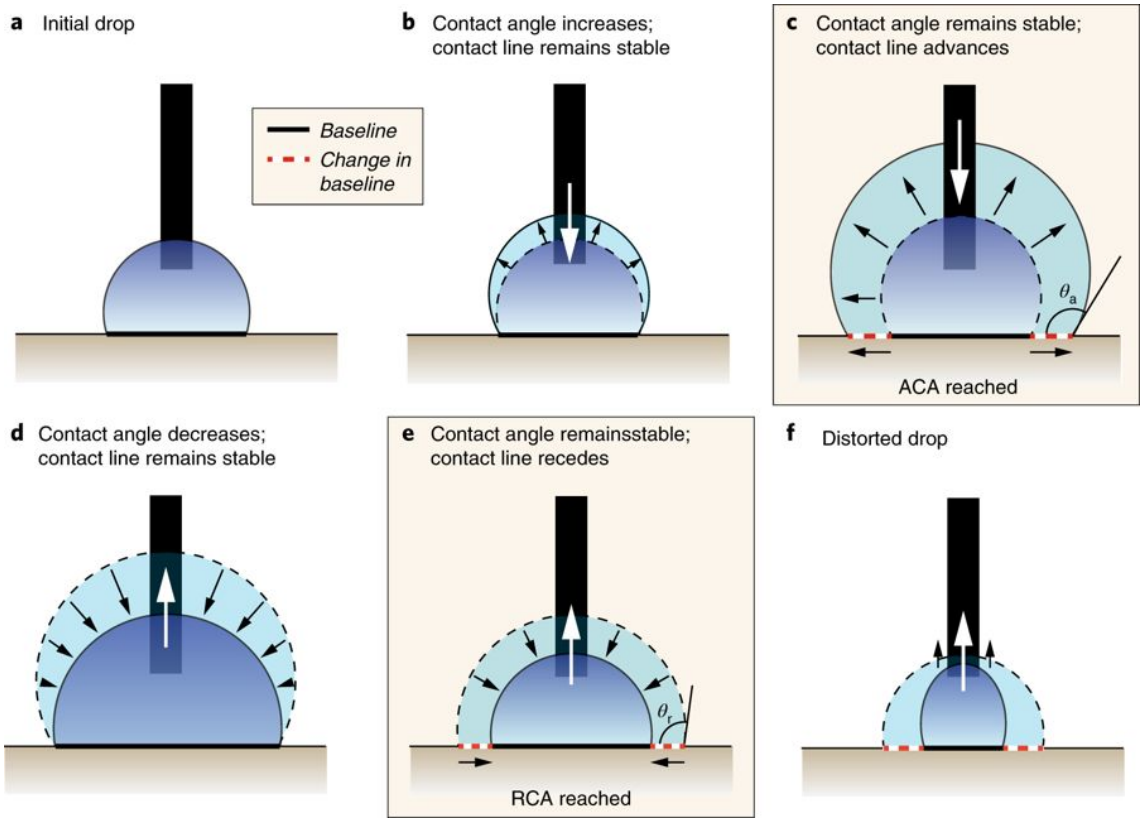

Figure 7: Sessile drop technique. The white arrows represent the water flow in the pipette. The ACA and RCA are reached in stages c and e, respectively. a, An initial droplet is deposited. b, Water is added to the drop before the measurement is started. At this stage, the ACA is not necessarily reached: the shape of the droplet changes, but the baseline remains stable. c, The ACA is reached, the baseline advances steadily as water is added, and the droplet volume increases while a video is recorded. d, In RCA measurements, water is first removed from an initial drop before recording of the video is started. At this stage, the RCA is not yet necessarily reached; the shape of the drop changes, and the baseline remains stable. e, RCA is reached, and the baseline recedes steadily as droplet volume is decreased while a video is recorded. f, A droplet smaller than 3 μL becomes distorted by the needle and the data are not reliable. Adapted from [40].

In the sessile drop technique, a droplet of water is deposited on a solid substrate. To measure the ACA, water is pumped in at a slow rate with a pipette into the droplet. The volume will increase and the CA with it, until the droplet reaches a

critical volume and the baseline starts to move. The ACA is measured the moment the CL moves as shown in the previous section. The same method but while pumping the water out of the droplet is used to measure the RCA [40]. The sessile drop technique steps are illustrated in figure 7.

In the tilted plate method, the point of basile movement is reached while tilting the substrate on which a droplet is deposited beforehand, thus giving it its name. The plate is tilted gradually until a critical angle between an horizontal line and the substrate is reached. This angle (often called the roll-off angle or the sliding angle[32]) changes according to the droplet volume as it is driven by gravity. When the sliding angle is reached, the baseline starts to move and the ACA is reached for the advancing meniscus and the RCA is reached for the receding meniscus. A representation of the droplet moving when the sliding angle is reached is shown in figure 8.

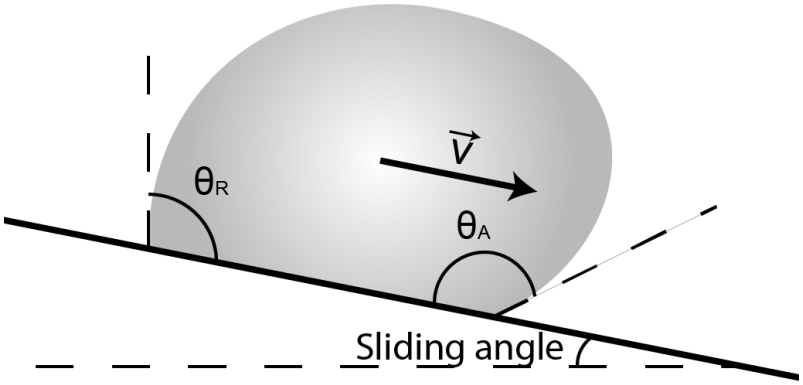

Figure 8: Tilted plate technique. Advancing contact angle θ_A is observed when the contact line advances to a non-wetted area and receding contact angle θ_R when the contact line recedes from a wetted area. Here, the sliding angle was just reached by the substrate, allowing the movement of the droplet with a speed v.

These two methods are dependent of the resolution of the camera used and of the fitting of the droplet shape. For superhydrophobic surfaces, the errors due to a misplaced baseline by one pixel, can be more than 2° for CAs around 150° and keep increasing exponentially with increasing CAs, even with a high resolution camera [42]. Even for hydrophobic surfaces, these techniques are not perfectly accurate. Other methods use force measurements instead of direct CAs measurements. One of the oldest and still widely used is the Wilhelmy plate method.

2.4.2 Wilhelmy Plate Method

The Wilhelmy plate tensiometry is a force-based measurement method. A thin plate of material can be investigated with this technique. The plate is linked to a tensiometer and is immersed in liquid. The force F is exerted on the plate through capillarity and hydrostatics is equal to :

$$F = \gamma(2d + 2W)cos(\theta) - V\Delta\rho g \tag{24}$$

Where V is the volume displaced by the plate, $\Delta\rho$ is the difference in density between the liquid and the air, g the gravitational acceleration, d and W are respectively the thickness and the length of the plate. The figure 9 gives a representation of the method.

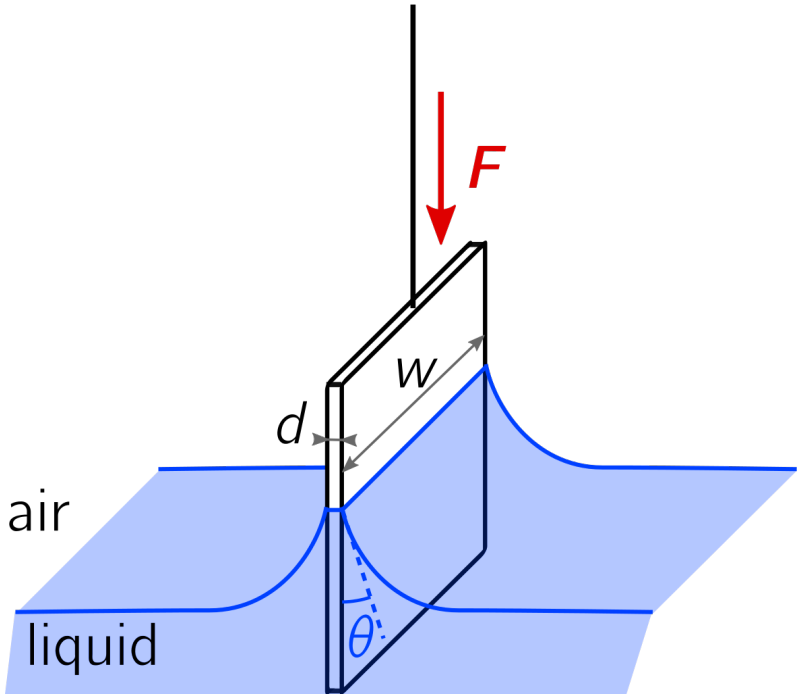

Figure 9: Illustration of Wilhelmy plate method. The force F is a combination of capillary force and hydrostatic force. The magnitude of the capillary force on the plate is proportional to the wetted perimeter, and to the surface tension γ of the liquid-air interface. Taken from **wilhelmy**

With this technique, the ACA can we calculated from the previous force expression when the plate is immersed in the liquid, and likewise, the RCA can be calculated when the plate gets pulled out from the liquid [43]. This technique gives accurate values if the sample is fully homogeneous in its wetting properties as well as its geometry. This technique has the benefit of not depending on cameras and can thus be more precise in some cases, notably for superhydrophobic surfaces [44].

There exist a few problems not addressed by these characterization techniques. For CA goniometry, the errors are quite high for superhydrophobic surfaces and it lacks precision. Also, these are relatively slow techniques if a mapping of the wetting properties needs to be made over the whole surface of a material. It would take repetitive measurements taking few minutes each[40]. As for the Wilhelmy plate method, even if it provides accurate results, it does not give information on the inhomogeneities of the materials and is thus not efficient for a local mapping of the wetting properties. New techniques were invented recently in order to provide maps of the wetting properties of a surface in a more precise and faster way.

2.4.3 Scanning Droplet Adhesion Microscopy

The Scanning Droplet Adhesion (SDAM) is a technique using force-based measurements to create a map of the wetting properties of hydrophobic surfaces at the microscopic scale [27]. The method consists of the following steps.

1. A water droplet is suspended from a force probe of high precision as the surface sample is placed under it.
2. The substrate is elevated until it touches the water droplet.
3. When the contact happens, a negative force called the *snap-in force* which is related to the ACA is exerted on the droplet.
4. The substrate is then lowered gradually.
5. During the retraction, when the droplet loses contact with the substrate, a *pull-off force* is measured, which is related to the RCA[45].
6. Iterations of the previous steps can be done after changing locations until a wetting map can be made. The spacing between measurements is usually of 200 microns.

These tests are done until a two-dimensional image of the surface's repellency can be made, called a wetting map. These steps are pictured in figure 10. This technique can be used to link microscopic features and topography directly to wetting properties and thus can lead to improved understanding of the phenomena at work.

2.4.4 Oscillating Droplet Tribometer

The Oscillating Droplet Tribometer (ODT) is a wetting characterization technique measuring on the dissipating forces applied on a droplet of water when it is moved on top of superhydrophobic surfaces [28]. Previous techniques making use of gravitational forces probed the dissipation forces when a droplet is moving on a superhydrophobic surface. Unfortunately, in these methods, the lateral and normal forces cannot be controlled independently [46]–[48]. The ODT manipulate of permanent magnets to control the movements of a water droplet containing a magnetic suspension (or ferrofluid) to produce oscillations in a magnetic well. The method consists of the following steps.

1. A ferrofluid droplet is deposited on the surface sample to test.
2. An auxiliary magnet is placed under the droplet in order to pin it while another magnet (the main one) is placed at a defined distance away from the droplet under the substrate.
3. The auxiliary magnet is removed, leading to a magnetic force pulling the droplet towards the main magnet axis.

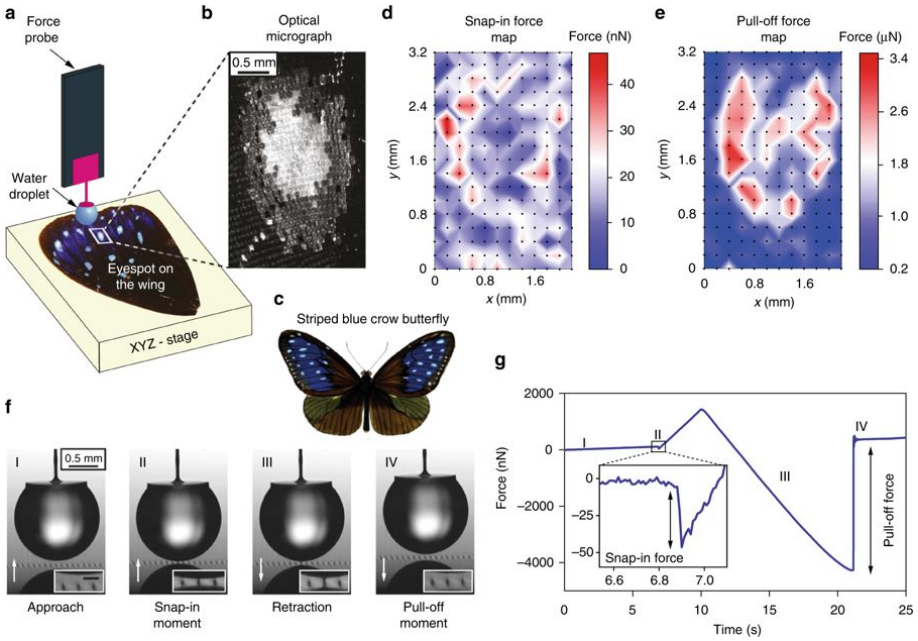

Figure 10: Concept of scanning droplet adhesion microscopy. a Schematic diagram of the microscope (not to scale). b Optical micrograph of scanned eyespot area on the wing of c, striped blue crow butterfly (typical wing span of adult specimen 80–90mm; image by Frederic Moore, PD-1923); with corresponding d snap-in and e pull-off force maps. Dots on d, e denote the measurement points with 200m spacing. Colours in the maps denote measured force values, linearly interpolated between the data points. f Snapshots of individual measurement on a single hydrophobic 5m radius pillar (white arrows indicate direction of sample surface movement, inset scale bar 70m), and g corresponding typical force curve. Roman numerals in f, g indicate corresponding moments in the measurement. Adapted from [27].

4. The droplet engages in oscillations around the main magnet axis, which are dampened by the dissipation forces until the droplet stops on the magnet axis.

5. The movement of the droplet is recorded with a camera and the motion is analyzed with a computer.

The forces applied to the droplet are pictured in figure 11. Two main dissipative forces are involved in the damping movements. The CAH-force F_{CAH} and the viscous force F_η which are defined by the equations [21], [49]:

$$\mathrm{F}_\eta = 2\beta\frac{dx}{dt} \quad \text{and} \quad \mathrm{F}_{CAH} = \frac{l}{2}\gamma_{lg}(cos(\theta_R) - cos(\theta_A)) \quad (25)$$

With β the viscous factor of the ferrofluid, and l the length of the CL. The external magnetic force F_{ext} is defined by :

$$F_{ext} = -kx \quad (26)$$

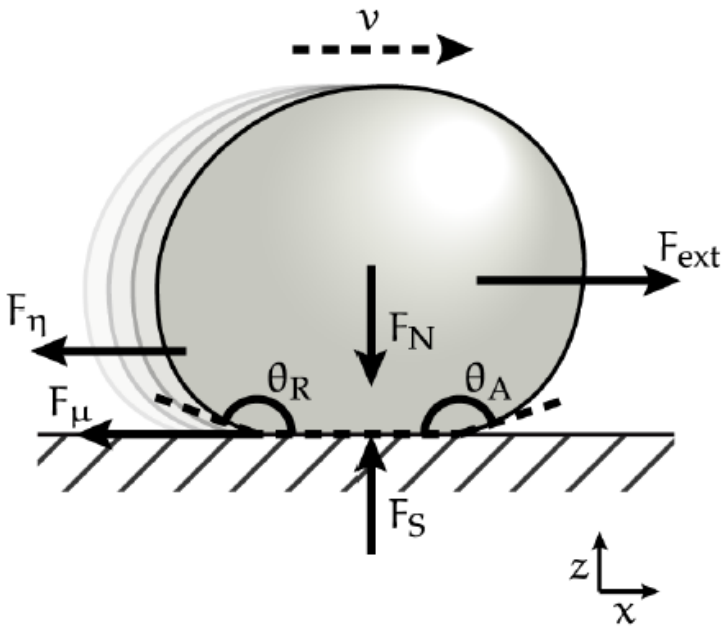

Figure 11: Forces acting on a ferrofluid droplet moving at velocity v on a superhydrophobic surface. F_{ext} is the magnetic force, $F_C AH$ and F_η the dissipative CAH-force and viscous force, respectively. F_N is the normal force due to gravitational and magnetic forces, and F_S the support force from the substrate. Taken from [28].

Where x is the distance between the droplet center and the magnet axis and $k = \mu_0 V c(M + H(dM/dH))$, with μ_0 the vacuum permeability, V the volume of the droplet, c the magnetic field curvature ($c > 0$), M the magnetization and H the magnetic field. The resulting magnetic field H has the spatial dependency of $H = H_0 - c\frac{x^2}{2}$, where H_0 is the field strength on the axis. Those forces are fitted with the solution of the general harmonic oscillator :

$$m\left(\frac{d^2x}{dt^2}\right) = -kx - F_\eta \pm F_C AH \tag{27}$$

Where the sign before $F_C AH$ is + if the droplet is moving left and − if the droplet is moving right. In the method, the fit concurred with the experimental results with high accuracy and thus allowed to measure the retentive force induced by the CAH efficiently. This method is particularly well-suited for measuring dissipative forces on the nN scale.

The SDAM and ODT methods were both developed in the Soft Matter and Wetting group in Aalto university, and the new characterization method introduced in this work is directly linked to these.

3 Research Material and Methods

There has been a few attempts to characterize wetting properties inside tubes using capillary forces but none have been successful for characterizing surfaces with CA greater than 90 degrees [50], [51]. We introduce a new technique called Scanning Droplet Tribometer to test hydrophobic transparent tubes.

3.1 Principle of Scanning Droplet tribometer

The principle of the scanning droplet tribometer is shown in Fig.12. It uses magnetically controlled water-like droplet to detect surface defects such as inhomogeneities in chemical composition or specific roughness which can change wetting behavior locally (as seen in Wenzel or Cassie-Baxter models). The technique measures the dissipation forces exerted on the droplet thanks to the magnetic force induced by two magnets.

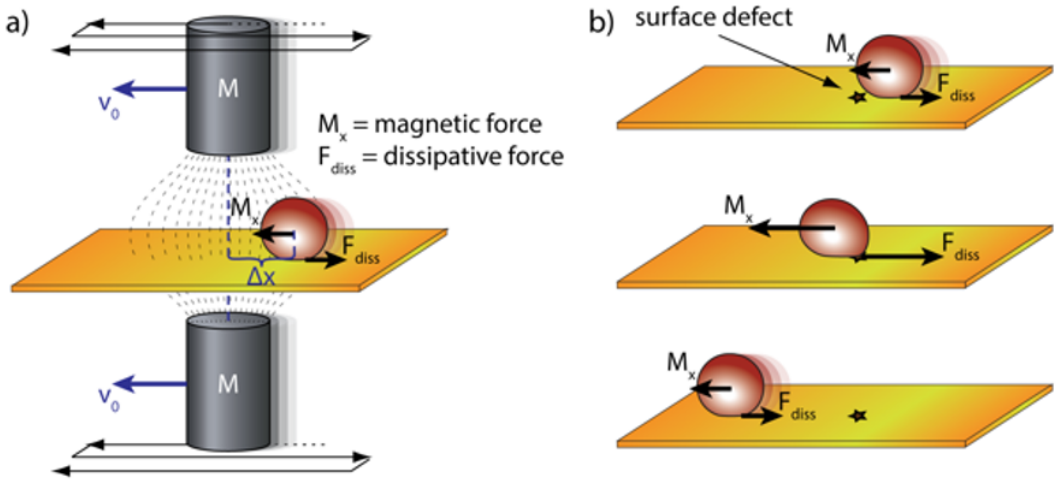

Figure 12: Scanning droplet tribometer principle. a) Cylindrical permanent magnets are moved horizontally at a constant velocity v_0, pulling the magnetic droplet along. Distance between the magnets' vertical axis and the center of the droplet Δx depends on the pulling magnetic force M_x and dissipative force F_{diss}. b) When the moving droplet encounters a surface defect(top), its receding edge gets pinned to the surface and an increased force is required to free the droplet (center). After the droplet is detached from the defect, it continues to follow the magnet (bottom). Credits: Mika Latikka.

Calculations are based on equation projected on the lateral axis:

$$F_{ext} = F_{mag} - F_{diss} \tag{28}$$

Where:

$$F_{diss} = F_{\eta} + F_{CAH} \tag{29}$$

And [52][28]:

$$F_{CAH} = kL\gamma_{lg}(cos(\theta_{Rear}) - cos(\theta_{Front})) \tag{30}$$

$$F_{\eta} = 2\beta\frac{dx}{dt} \tag{31}$$

Where k is a dimensionless factor account for the shape of the three-phase CL and L a representative length of the droplets. The other parameters were introduced in the ODT section. According to the authors of the ODT [28], the magnetic force can be described by:

$$F_{mag} = 2(-\mu_0 Vc(M + H(dM/dH))|x_{droplet} - x_{magnet}|) \tag{32}$$

Since magnetic field are cumulative, the magnetic force is doubled compared to the ODT because there are two magnets. When the droplet is pinned by a surface defect, it becomes immobile: $F_{ext} = 0$ and $F_{mag} = F_{diss}$. The pulling magnetic force increases due to the magnets moving away from the droplet and the droplet follows the magnets when $F_{mag} > F_{diss}$. After a short time, the maximum of magnetic force is reached and the droplet starts moving, $F_{mag} = F_{CAH}$ and the CAH-force is equal to :

$$F_{CAH} = kL\gamma_{lg}(cos(\theta_{Receding}) - cos(\theta_{Advancing})) \tag{33}$$

Values for k were calculated between $1/2$ and $\pi/2$ [53]–[55]. In this work, we simplify the previous equation by assuming a constant value $k = 1$. The angles $\theta_{Receding}$ and $\theta_{Advancing}$ are not known because of the difficulty to set a proper baseline in this setup. However, the value of L is known at every moment, as it is measured thanks to custom functions in MATLAB and assimilated to the length of the receding CL. The geometry characterized is not a plane surface but a tapered tube. The droplet wet the whole circumference of the samples due to their low size and due to capillary effects. These effects do not affect lateral force, the technique is thus directly applied to this geometry. As opposed to a plane surface, where the defects positions are known, the defects can be present at any position on the radius of the sample and thus only the lateral positions of the defects are investigated here.

3.2 Hydrophobic Tapered Tubes

Surface characterization of transparent low retention tapered tubes with the scanning droplet tribometer were made. We used two type of samples with supposedly different wetting surface homogeneity.

3.2.1 Samples : Small Tapered Tubes

Fabrication of tapered tubes was done using polypropylene with water repellent additives in an injection molding process. The dimension goes from a small orifice of diameter r_1 to a big orifice of diameter r_2 (where $r_1 < r_2 < 1.5mm$) over a length of $D = 28.5mm$. A second set of samples were manufactured with the same protocol

but were additionally annealed for one hour at 130°C at the end. Both sample types are transparent. The sample geometry is represented in Fig.13.

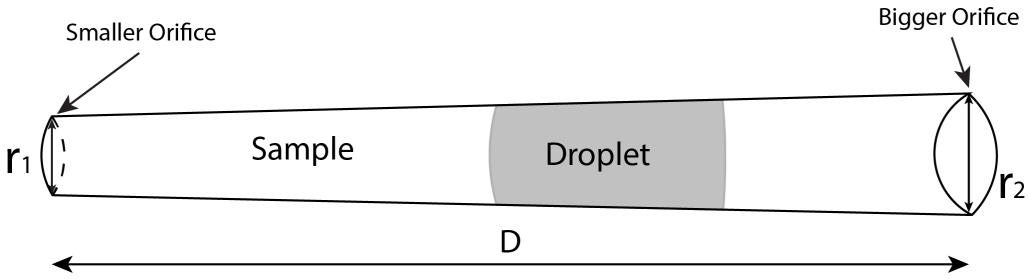

Figure 13: Representation of the small tapered tube. D is the length of the sample, r_1 is the diameter of the smaller orifice and r_2 is the diameter of the bigger orifice. The testing droplet is also shown in the sample to show its transparency.

3.3 Ferrofluids

Two test liquids were used in the experiments : water and Phosphate-Buffered Saline (PBS) solutions with a small amount of superparamagnetic iron oxides nanoparticules (2 vol%). The PBS buffer solution is composed of 5% PBS and the 95% water with a pH of 7.4. The obtained magnetic fluids are called ferrofluids. Ferrofluids are colloidal suspensions of magnetite of maghemite nanoparticles. The added nanoparticles allows the fluid to obtain magnetic properties and to be remotely controllable with magnetic fields. In these solutions, the minute amount of nanoparticles added to the fluid does not change much the physical properties of water, such as density or surface tension. The PBS is also an aqueous solution which properties are close to that of water.

3.3.1 Synthesis

The synthesis of nanoparticles was made using the same recipe as in [28]. Iron oxide nanoparticles were synthesized by coprecipitation method in water and stabilized with citric acid near pH 7 [56]. First, an aqueous mixture of ferric chloride (FeCl3 6H2O) and ferrous chloride (FeCl2 4H2O) was prepared (mixture ratio FeCl3/FeCl2 = 2:1). Magnetite (Fe3O4) nanoparticles precipitated from the mixture after adding ammonia (NH4OH) and stabilizing with citric acid. The resulting solution was then sequentially washed with Milli-Q water and acetone and concentrated via magnetic decantation until the density was close to 2g/ml (exactly 1.938g/ml), which corresponds to nanoparticle concentration of 20vol-% (exactly 22.068vol-%). The concentrated ferrofluid was subsequently diluted to achieve the test liquid with 2 vol-% nanoparticle concentration. In a previous work, the nanoparticles synthesized with the same method were characterized with a transmission electron microscope (JEOL JEM-2200F, 200 kV). The average particle size was 4.6 nm with a geometric standard deviation of 1.4nm [28].

3.3.2 Magnetic Properties

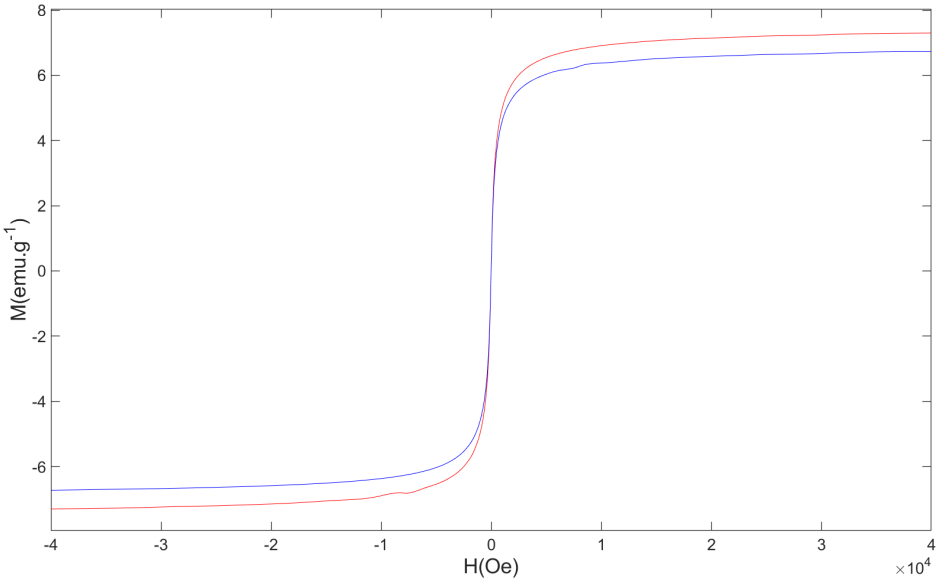

Figure 14: Magnetic properties of the 2 vol-% iron oxide nanoparticle dispersions. Magnetization curves from -4 to 4 kOe at room temperature. The blue curve is the magnetization curve of the PBS-based ferrofluid and the red curve is the magnetization curve of the water-based ferrofluid.

The magnetic properties of the dilute ferrofluid was measured with a SQUID magnetometer (Quantum Design MPMS XL7). Hysteresis curves were measured by placing approximately 10 of the ferrofluid was in a 3-mm NMR tube, which was heat-sealed with a polypropylene cap. The sample magnetization was measured using reciprocating sample configuration with background subtraction option between - 4 kOe to + 4 kOe in room temperature. No magnetic hysteresis was detected (Fig. 14).

3.3.3 Surface Tensions

Surface tensions of both dilute ferrofluids were investigated using pendant drop method for more than one minute using an optical goniometer (DATAPHYSICS OCA_{20}) with NORDSON PRECISION TIP 7018062 needles with outer diameter of 1.65 mm. The average surface tension for the water-based ferrofluid was 71.6±0.03 mN/m while the average for the PBS-based ferrofluid was 73.1±0.03 mN/m. In addition, the surface tensions of both ferrofluids remained constant during the measurements, indicating that the solutions are stable other this time period and that the nanoparticles does not migrate to the liquid-air interface.

3.4 Hardware

The experimental setup was built to magnetically control a ferrofluid droplet inside a tapered tube and to record the motion inside the transparent tube. It consists of two main parts: a hardware and a software. The hardware is used to manipulate the magnetic droplets between two cylindrical magnets (KK MAGNET-ICS, NdFeB N52) using a moving linear stage and the movement is recorded with a camera. The software provides tools for image analysis.

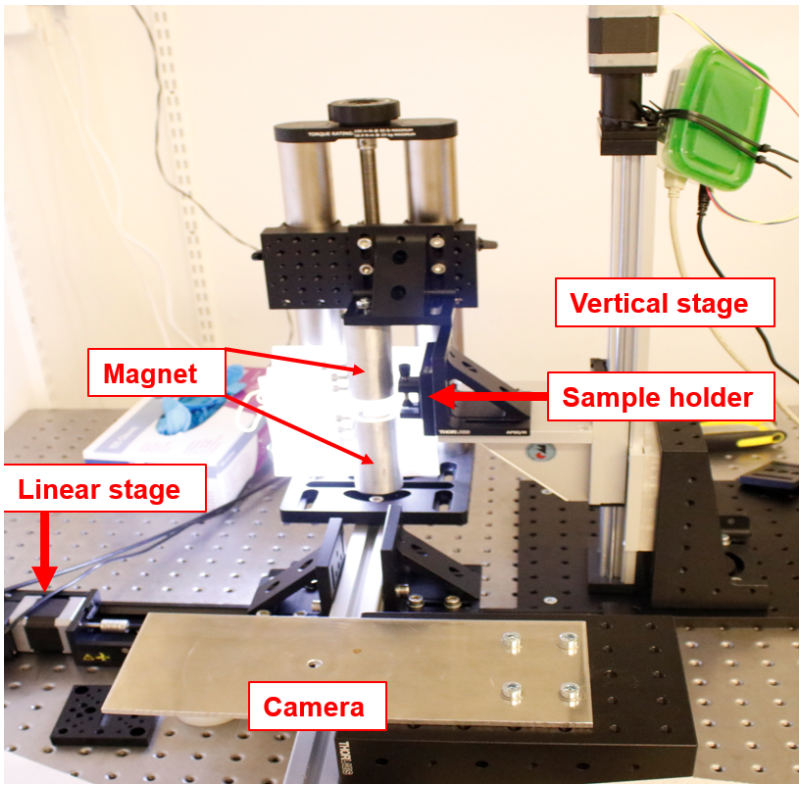

Figure 15: Picture of the experimental setup hardware. The linear stage is controlled with a computer and moves the magnets as well as the camera. The vertical stage allows to precisely place the sample with an ARDUINO controller. The sample is immobile when the magnets are moved, leading to the ferrofluid in the sample moving towards the magnets vertical axis and scanning the surfaces of the tapered tube.

The hardware consists of a linear stage (ZABER X-LSQ300B), two uniaxial cylindrical permanent magnets (KK MAGNET-ICS, NdFeB N52), a camera (CANNON 80D with Sigma 105mm f/2.8 EX DG Macro Lens) and a sample holder. The magnets are attached to the setup symmetrically below and above the sample which is fixed. A LED wall with a screen in front of it is placed behind the sample to obtain a uniform background. The magnets create a magnetic field, which is used to apply vertical forces on a magnetic test droplet. On the other hand, horizontal magnetic force will be close to zero, leaving the normal force and droplet shape unaffected. The magnets and the camera are attached to the linear stage, which allows scanning

of the tapered tubes with magnetic droplet on their whole length. A picture of the hardware is given in figure 15.

3.4.1 Measurement Procedure

The tests methodology is as follow : 1.5 μL of ferrofluid is pippeted in the sample at the bigger orifice position, then, the tube is fixed to the sample holder of the setup with the droplet being in the same vertical axis as the two magnets. The magnets are moved at a speed of 1mm/s for 35mm to the left, then to the right thanks to the linear stage and using the ZABER CONTROL software. These steps are done at least 3 times without changing the ferrofluid in the sample (3 back and forths). The motion is recorded at HD quality 1920x1080 pixels and at a speed of 60 frames per second. The motion videos are then analyzed with a Matlab program using custom functions.

3.5 Image Analysis Program

The image analysis program was custom made specifically for this project. It identifies the droplet and its position at all time, calculates the distance between the droplet and the magnet axis and calculate the forces along the tube. The image analysis program was based on the program developed in the ODT but it was not sufficient for our technique. Indeed, in the ODT, the droplet was moved on a flat surface while the samples used here are curved surfaces. It leads in the baseline detection not working anymore and the droplet could no be identified with precision. Also, the camera is now moving with the stage and the coordinates need to be recalculated. Thus, the luminosity threshold, the image cropping and calculation of magnetic force were taken from the ODT but the rest was revised.

4 Results and Discussion

The scanning droplet tribometer was used to characterize the wetting properties of two types of tapered tubes using two different ferrofluids.

4.1 Results

First, only the water-based ferrofluid was used in the experiments. The previous methodology is used: three times right to left and left to right water-based ferrofluids sweep tests were conducted for each sample. In the Fig.16 is plotted the curve of dissipation forces in function of time for the annealed tapered tube using the water-based ferrofluid when moving the magnets from the big orifice to the small orifice.

There is four different periods in this test represented in Fig.16.a) :

I The camera starts recording and both the droplet and the magnets are immobile.

II The magnets start to move, it goes from right to left in this test towards the droplet and will be in the same vertical axis of the droplet at the end of the section leading to a magnetic force equal to $0N$.

III The magnets pass the droplet and the droplet starts to follow the magnets in spurts, it is where the meaningful data is retrieved.

IV The droplet reach the other end of the tube and the test stops.

The Fig.16.b) shows a magnification of the curve in Fig.a) within the red rectangle. There is two regimes in this curve :

I In the first regime, the droplet is in a static state, the droplet is immobile, pinned by retention force and inhomogeneities and the magnets are moved further away from the droplet, leading to an increased in the magnetic force. During this regime, the curve is directly driven by the equation (since there is no motion by the droplet, $F_\eta = 0$) :

$$F_{mag} = F_{CAH} \tag{34}$$

At each peak, F_{mag} is given by equation 32 and F_{CAH} is given by equation 33. Thus, at each peak, we can calculate from the curve the wetting properties of the surface (*i.e.* the CAH) since we know the surface tension of the ferrofluid and the CL length is given by the program at each position.

II In the second regime, the magnetic force is higher than the dissipation forces and the equilibrium is broken : the droplet moves. The droplet is then pinned again where the dissipation forces are equal to the magnetic force which is reduced because the droplet moved toward the magnets (see equation 32). We are now back in regime I). The second regime gives us information on a value of the sum of both dissipation forces and thus of on the maximum of retention force possible. These alternative regimes happens during all the measurements, and is the same even for smaller peaks.

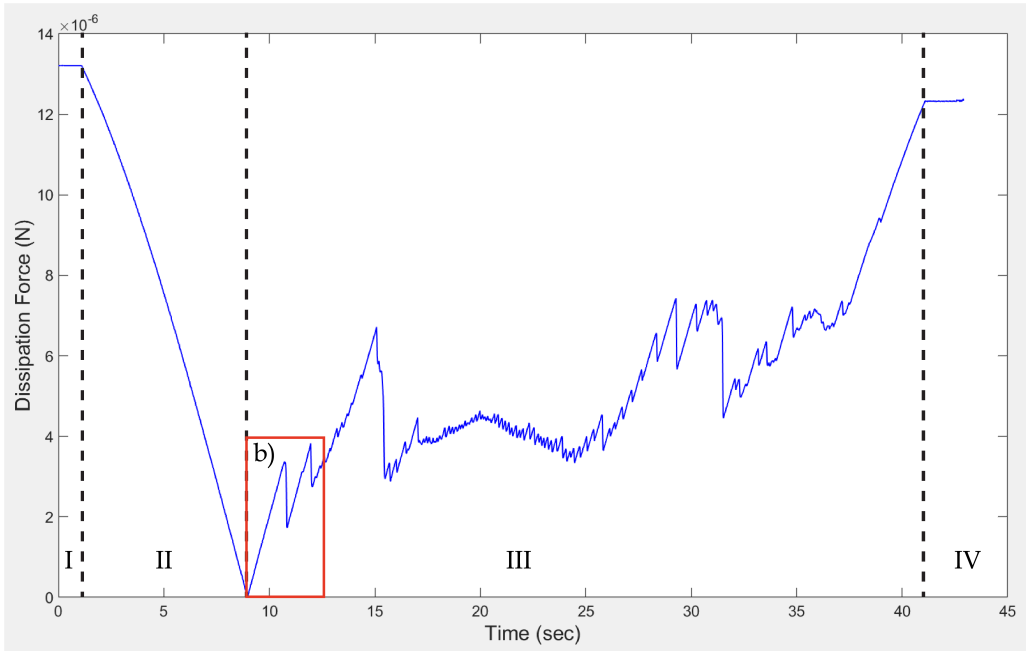

(a)

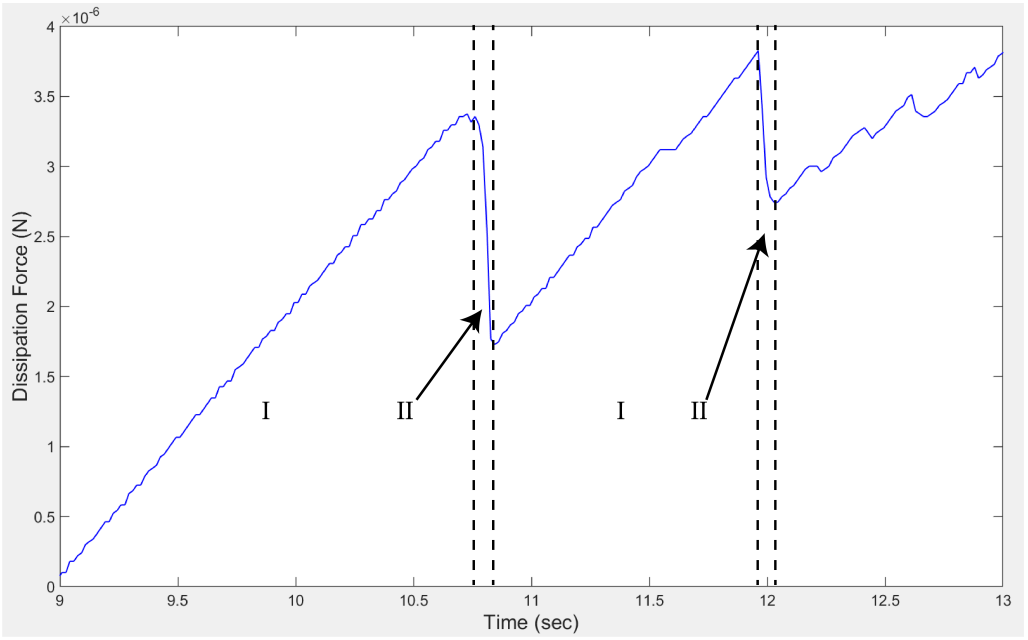

(b)

Figure 16: Curve of Dissipation Forces in function of Time. Fig. 16.a) show the dissipation forces (in Newtons) as a function of time (in seconds) for a typical measurement with the scanning droplet tribometer. Fig.16.b) shows the magnification of the red rectangle in Fig.a).

This is a typical curve and an general example with time as abscissa axis. A second significant plot can be done with the position in the tube in mm, meaning the position away from the bigger orifice of the tube in this case. The force curve is plotted with the distance between the bigger orifice of the tube and the position of the droplet (the position of the receding CL to be exact), in figure 17.

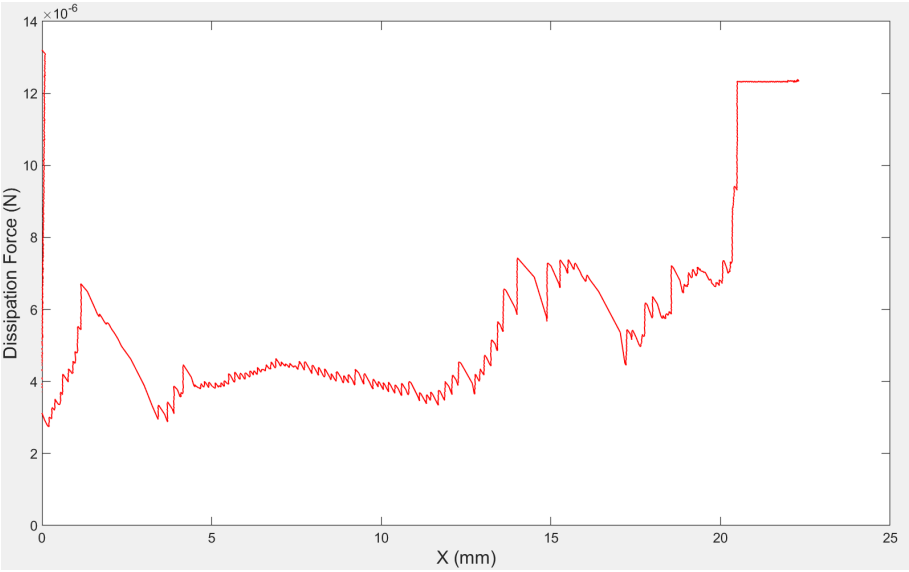

Figure 17: Curve of Dissipation Forces in function of the distance between the tube bigger orifice and the droplet.

The tube is longer than the distance X seen here. The test stops here for $X = 21mm$ and the values shown after it on the graph can be discarded; while the tube is 28.5mm long. It can be explained by the fact that we look here at the receding CL position and not the advancing CL position. Now looking at the results, it appears that the tube has quite homogeneous wetting properties from $X = 4mm$ to $X = 13mm$ with a retention force of about 4 μN, while there is a strong inhomogeneity when X range from 0 mm to 4 mm, and another one from 13 mm to 17 mm.

Before going forward with other results, the Reduced Retentive Force (RRF) is introduced. It is more relevant to our system because it takes into account the CL length in the force. It is derived from equation 33 [57] :

$$\frac{F_{CAH}}{L\gamma_{lg}} = (cos(\theta_R) - cos(\theta_A)) \tag{35}$$

As reminder, we previously set k=1, thus it is not included in this equation. What we call the RRF is the fraction $\frac{F_{CAH}}{L\gamma_{lg}}$. It is dimensionless and includes the geometrical effects of the CL length directly in the force. For convenience, future force curves will assimilate the total dissipation forces as retentive force only. It is important to keep in mind that it is only true at peak positions. Furthermore, instead of plotting the retentive force, we will plot the RRF which was introduced in equation 35.

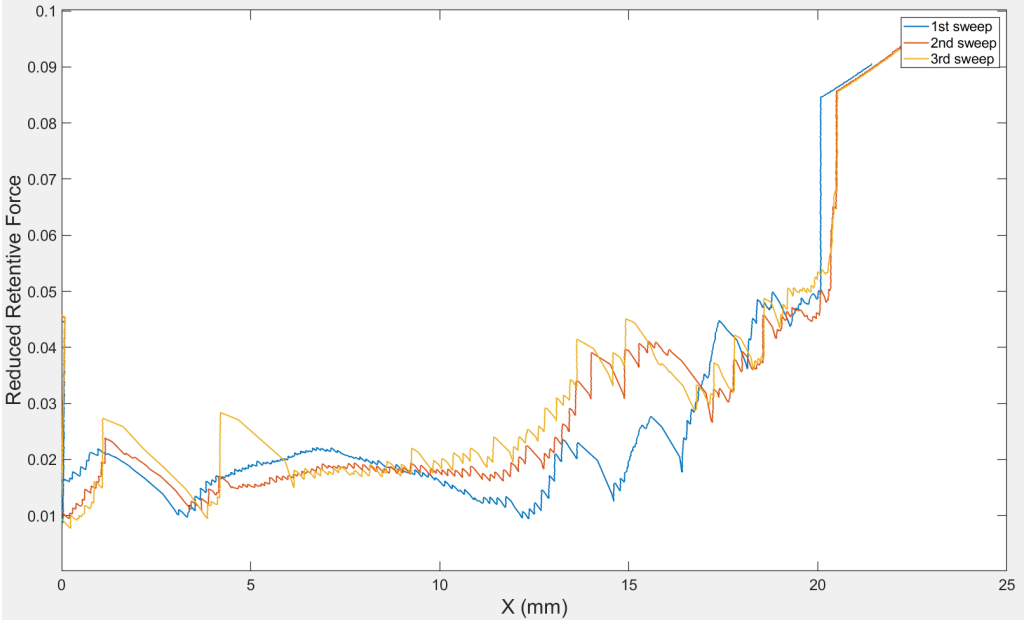

Figure 18: Curves of reduced retentive force in function of distance between the tube bigger orifice and the droplet position on the x-axis. The blue curve is the first sweep, the yellow curve is the second sweep and the orange curve is the third sweep.

For the same sample, a test following the methodology given in section 3.3.1 was conducted with water-based ferrofluid. The RRF curves calculated from the three sweeps starting from the right position and ending to the left position are given in Fig.18.

A noticeable feature given by this figure is the difference between the first sweep and the others. Indeed, while the second sweep and the third sweep are quite similar, the blue curve is shifted, especially around $X = 15mm$. Even if it has the same pattern as the other curves, its peak values are around two times lower for the same peaks. The samples were not cleaned in any way before the test, so it is highly possible that the first sweep cleaned the surface from all possible dust.

Conversely, the RRF curves calculated from the three sweeps starting from the left position to the right position are given in Fig.19. Here $X_{L->R}$ stands for the distance in mm between the tube smaller orifice and the droplet position on the x-axis (which is the receding CL position and was the advancing CL for the other sweep test from right to left).

A quite large inhomogeneity increases the RRF around 8 mm away from the smaller orifice to 0.06. First of all, the test goes from $X_{L->R}$=0mm to 28mm which is almost the length of the tube as opposed to the previous test which stopped around $20mm$. It is explained by the fact that the distance X is measured between the sample orifice and the receding edge of the droplet for each test: in the test when the magnets are moved from right to left, the receding meniscus is located to the right of the droplet and it is reversed for the test from left to right.

The first sweep here is again quite shifted from the second and third sweeps. Maybe because some impurities are left on the surface. Also, it is expected from the

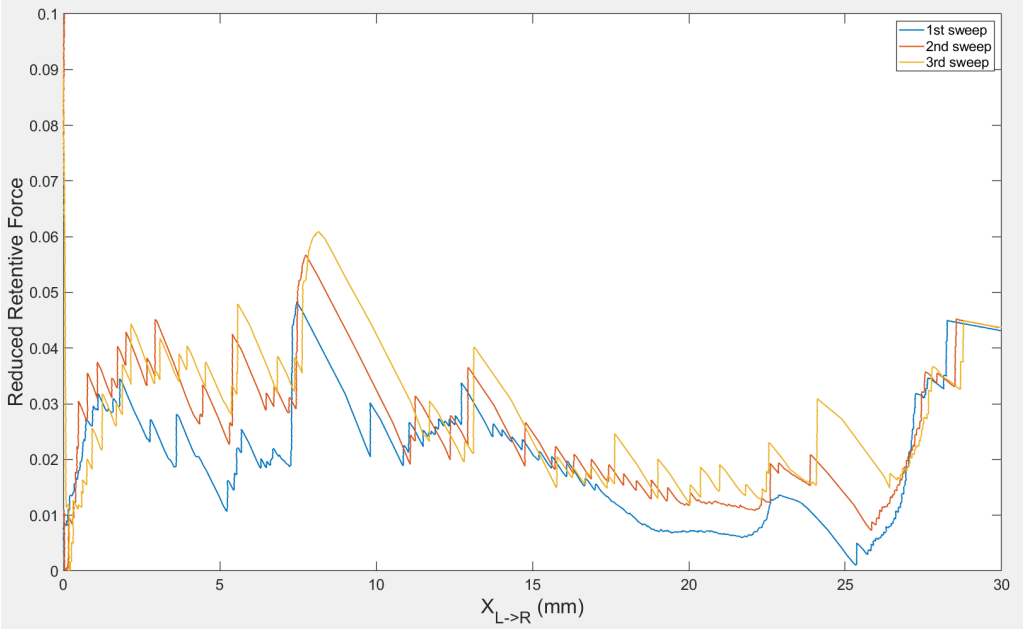

Figure 19: Curves of reduced retentive force in function of distance between the tube smaller orifice and the droplet position on the x-axis. The blue curve is the first sweep, the yellow curve is the second sweep and the orange curve is the third sweep.

theory that the position of the pinning sites are the same as their positions should not depend on the sweep direction. To prove it, a plot of the RRF in function of the distance between the smaller orifice and the receding edge for both sweeps is plotted. To do it, the X coordinates of the right to left sweep are inverted and shifted to fit the shape of the right to left sweeps curves. The forces remained unchanged. The result is given in Fig.20.

The starting position of the left to right sweep test is pictured in Fig.21 for further clarification. The relevance of the shift used to the actual sample is verified.

The shift between the blue curves and the red curves is equal to h in Fig.20 which is the length of the droplet in the x-axis. It is equal to 7.7mm in this configuration in order to have nicely tuned curves. If we calculate the volume of the droplet assimilated to a circular truncated cone which is given by equation :

$$V = \frac{h\pi}{3}(r_1^2 + r_1 r_2 + r_2^2) \tag{36}$$

We obtain a volume 1.7ul for the droplet, which is coherent with the droplet we introduce at the beginning of the test of 1.5ul, while being a bit oversized.

As seen in Fig.20, the blue curves and the red curves fit relatively well. The RRF values are similar for every X and the main inhomogeneities can be seen for both tests : around $X = 8mm$, $X = 13mm$, $X = 24mm$ and $X = 27mm$. As it was plotted according to the distance of the receding edge for each test, it is in accordance with [57] as the graph validates the fact that the receding CL is where the pinning occurs (because the peaks are at the same position no matter the direction of the movement).

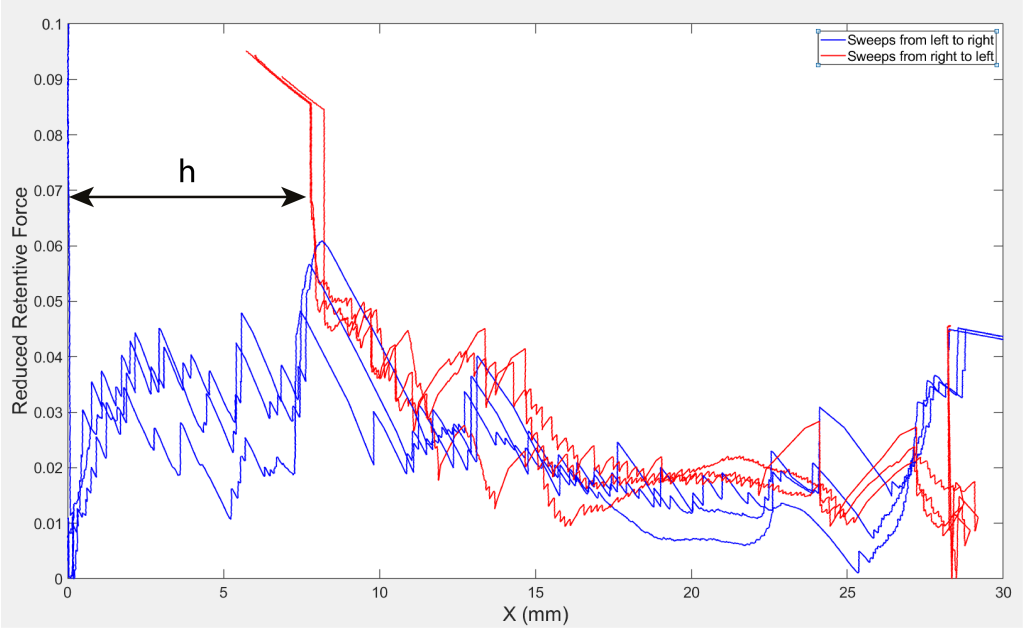

Figure 20: Curves of reduced retentive force in function of distance between the tube smaller orifice and the droplet receding edge position on the x-axis. The blue curves represented the sweeps from left to right while the red curves represent the sweeps from right to left but reversed and shifted in order to take into account the distance between the two edge of the droplet. h is the distance between the leftmost position of the droplet and the rightmost position of the droplet when it is at starting position of the left to right sweep test.

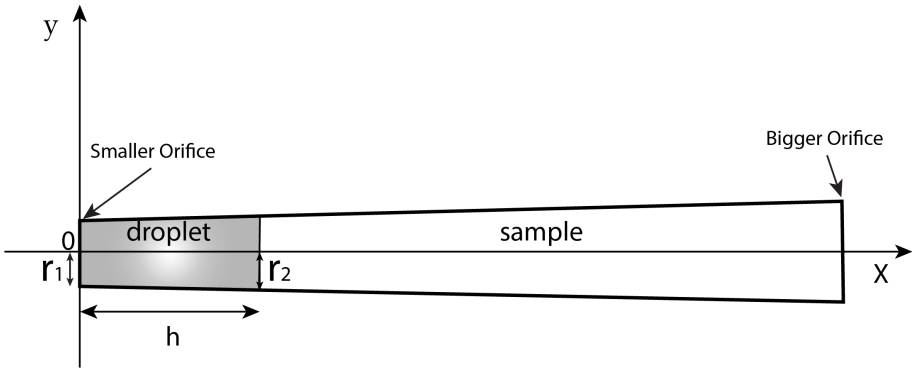

Figure 21: Representation of the sample when the droplet is at the starting position for the left to right sweep or the ending position of the right to left sweep. The h is the same as the one in figure 20.

As such, the sweep tests from left to right give wetting properties over the whole range of the samples, and the right to left sweep tests do not give information on the smaller part of the sample. Although sweep tests from right to left can gives complementary information on the samples, for the rest of this work, only plots of the sweep tests from left to right will be outlined.

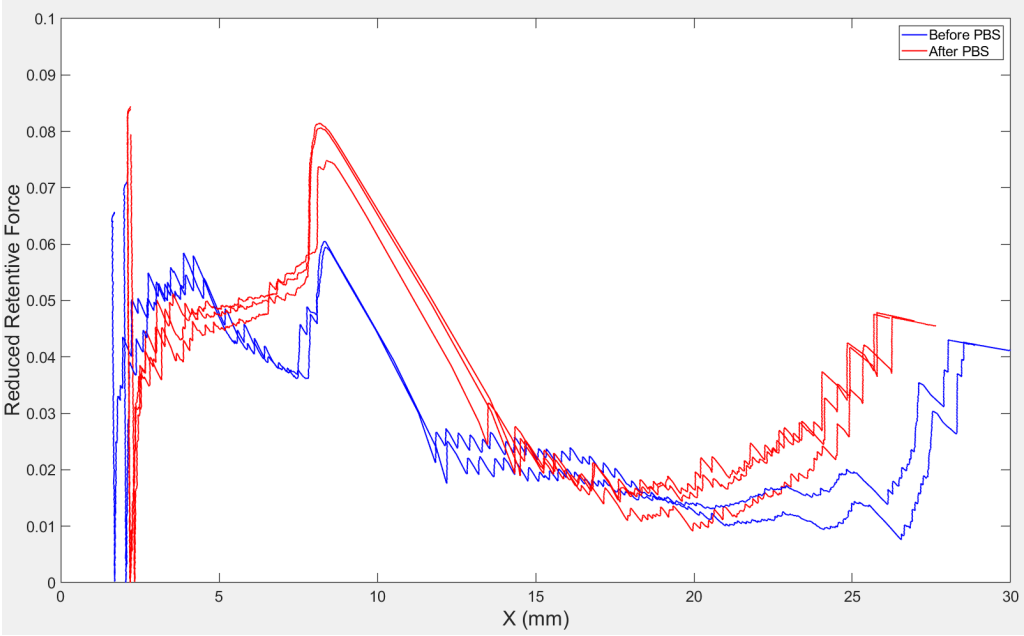

Figure 22: Left to right sweep tests with water-based ferrofluid before and after PBS-based ferrofluid sweeps on normal samples. The blue curves correspond to the water ferrofluid before the PBS ferrofluid sweeps and the red curves correspond to the water ferrofluid sweep tests after the PBS ferrofluid sweeps.

To test our two types of samples : normal and annealed tapered conical tubes, we use two different ferrofluids: water-based and PBS solution-based in a combined test. First, three times right to left and left to right sweeps are conducted with the water ferrofluid, then the liquid is removed from the sample. After that, three times right to left and left to right sweeps are done with the PBS ferrofluid, the liquid is removed from the sample. And finally, three times right to left and left to right sweeps are done with the water ferrofluid.

The RRF curves for the water ferrofluid sweep tests in function of the position from the smaller orifice are plotted in Fig.22 for the normal samples and in Fig.23 for the annealed samples. First of all, the blue curves representing the water ferrofluid sweep tests before the PBS ferrofluid sweep tests are of similar shape for both samples types. The curves increase to a RRF of 0.05 for annealed samples and of 0.04 for normal samples for X between 2mm to 8mm. Then a noticeable inhomogeneity is detected around $X = 9mm$ with a peak at 0.06 for both sample types. It is followed by a decrease to RRF=0.03 for the annealed samples and RRF=0.025 for normal samples. Then for both types of samples, the surfaces are relatively homogeneous with a small decrease in RRF until $X = 26mm$ where it increases again until the tests stop.

It results in normal samples having more inhomogeneities, especially around $X = 4mm$ where the values of RRF are higher. However, there is no clear distinction between the two from the water ferrofluid sweep tests before the PBS ferrofluid sweep tests, they both have a large inhomogeneity around $X = 9mm$ of similar values.

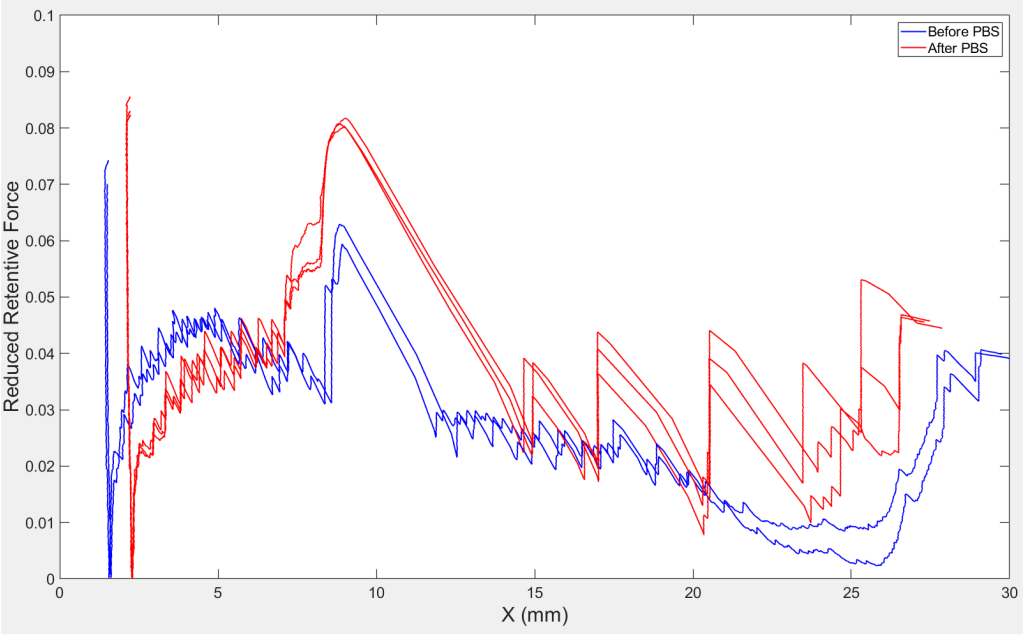

Figure 23: Left to right sweep tests with water-based ferrofluid before and after PBS-based ferrofluid sweeps on annealed samples. The blue curves correspond to the water ferrofluid before the PBS ferrofluid sweeps and the red curves correspond to the water ferrofluid sweep tests after the PBS ferrofluid sweeps.

Nonetheless, the water ferrofluid sweep tests after the PBS ferrofluid sweep tests (in red in Fig.22 Fig.23 show some differences between annealed and normal samples.

The first distinction can be made when X values are between 3mm to 8mm. The normal samples behave in the same way but the RRF increases when it approach the main inhomogeneity around $X = 9mm$ instead of the decreasing as before the PBS ferrofluid sweep tests. At the X of the main inhomogeneity, the value of RRF increases to 0.08 comaped to 0.06 previously. For the annealed samples, the curves of RRF are shifted to lower values in the beginning of the range X and increases at the main homogeneity to RRF=0.08 for $X = 9mm$ as the normal samples do. Like in the previous sweep tests, the RRF decreases, and for these tests for a longer distance X to X around 15mm for both curves. Then the two types of samples have really different behaviors. The normal samples follow the previous tests curves but the RRF increases earlier at $X = 20mm$ to finish the test at an lower X compared to previous tests. Indeed, it was visible on the video that the droplet did not reach the end of the sample after the PBS ferrofluid tests. For the annealed samples, the red curves seem to bounce on the blue curves to form a total of five main peaks reflecting five inhomogeneities on the surface which were not present for the water sweep tests before the PBS sweep tests.

These tests shown that the PBS ferrofluid had some impact on the surface of the samples, with a significant increase of retention forces for the main inhomogeneity for both samples at $X = 9mm$ and five peaks of inhomogeneities appearing only for annealed samples between $X = 15mm$ to $X = 27mm$.

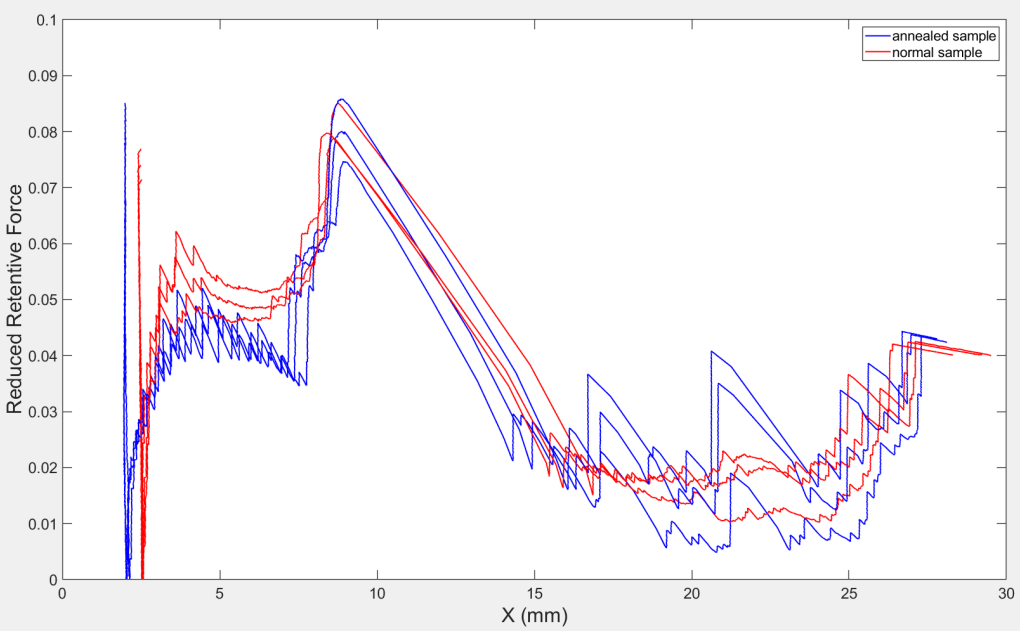

Figure 24: Left to right sweep tests with PBS-based ferrofluid. The blue curves correspond to the PBS ferrofluid sweeps on the annealed samples and the red curves correspond to the PBS ferrofluid sweeps on the normal samples.

The curves of RRF in function of X are also investigated for PBS ferrofluid sweep tests. There was no difference between PBS sweep tests between tests done before or after water ferrofluid tests so we give the curves of the ones done in the previously mentioned test (with water ferrofluid sweep before and after the PBS ferrofluid sweeps). The curves of RRF in function of X for annealed and normal samples are plotted in Fig24, with the blue curves corresponding to the annealed samples and the red curves corresponding to the normal samples. These curves are quite similar to the water ferrofluid sweep tests. For both annealed and normal samples, there is still this significant increase of RRF at $X = 9mm$ to a value of average 0.08 with a further decrease. Again some inhomogeneities are shown around $X = 15mm$ to $X = 25mm$ for the annealed samples, even if the peaks are not as clear as in Fig.23, and quite uniform wetting properties on the same range for normal samples. These also show that the RRF is bigger for normal samples in the first $X = 3mm$ to $X = 8mm$.

Thanks to the scanning droplet tribometer method, we were able to successfully prove that the PBS ferrofluid had an effect on the tapered tubes with different effects if the tubes was annealed of not. Both had an already existing peak of RRF around $X = 9mm$ even further increased after PBS ferrofluid was swept in the samples, while the annealed sample lost its relative uniformity in wetting properties from $X = 15mm$ to $X = 25mm$.

4.2 Discussion

A number of choices and assumptions were made in this paper and affect the results obtained.

First of all, decisions were made in order to make the measurements easier. A relatively strong background light was used in the setup, with an overexposed camera in order to make the tapered tube almost "invisible" and to make the droplet standout more thanks to its black color. It is shown in Fig.25. However, this leads to the droplet appearing smaller than it actually is. Even if morphological image processing techniques were used to minimize this effect, it is still a source of incertitude. The curvatures of the droplet were also not taken into account for the measurements of the CL length. Indeed, we simplified the droplet shape and assimilated it to a circular truncated cone and oversized the droplet.

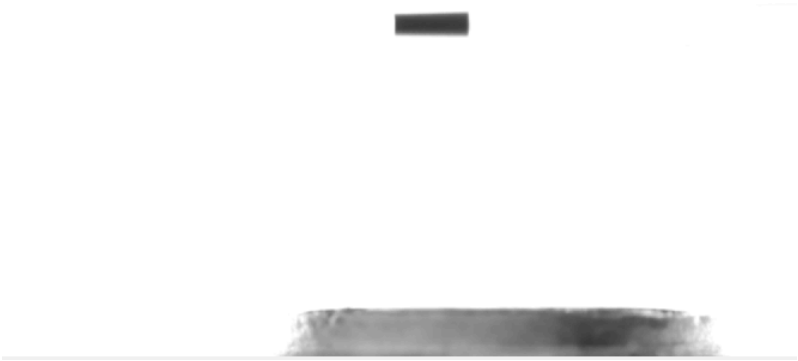

Figure 25: Image of the droplet during ferrofluid sweep test with strong light background. The droplet is located in the middle of the image with one of the two magnets at the bottom fo the image.

Modeling and shape analysis could be conducted through Surface Evolver or a similar software which is used for the study of surfaces shaped by surface tension and other energies, and subject to various constraints. It would allow to validate the model used during the calculations of the forces but also to accurately define the factor k and length L in the CAH-force in equation 33. Indeed, the redecing CL length was chosen as a representative length because most of the retention force happen at the receding edge[58] but it might not be the most optimal value. Thus, the modelisation would give more accurate values.

Furthermore, improving the reproducibility of the method seems important. As seen in the previous section, the starting position is not always the same when changing samples and need to be corrected manually. Also, the recording of the video is done manually and could be automated in order to trigger when the motion of the magnets is launched for more precision. Furthermore, cleaning the sample

beforehand could result in a first sweep closer to the following sweeps but could maybe influence in a unexpected way so it was not done in this work.

With these assumptions, especially the ones made on the F_{CAH} with k and L, it is not sure if the values we obtain are *absolute* values. Indeed, if we change the geometry of the sample for example, new k and L values need to be accessed and change the resulting retentive force. However, since our main topic of interest is discovering inhomogeneities and their relative magnitude, being able to do relative analysis is sufficient.

4.3 Future Work

This work open prospect in improving the surface wetting uniformity of more diversified surfaces, which is hard to measure accurately. It is possible to easily attain different degrees of sensitivity by modifying the percentage of nanoparticles in the ferrofluid or changing the volume of the test droplet. Indeed, if the percentage of nanoparticles is too high, then the droplet will never be pinned and sensitivity is lost, however, a too low nanoparticules concentration would result in the droplet not following the magnets. In this work, the concentration of nanoparticules was optimised to have a good sensitivity to the surface defects. It would also be possible to have stronger or weaker magnets to change the sensitivity but changing the ferrofluids properties or volume is more practical. The scanning droplet tribometer technique is still relatively new and would need some adjustments regarding the setup. But the main improvement would be to develop numerical simulations in order to define better the retentive force at play in this scanning droplet tribometer technique.

5 Summary

Hydrophobic surfaces, or water repellent surfaces, have interesting properties for applications on self-cleaning, anti-icing, antifogging and fluid drag reduction. To develop more efficient surfaces, proper characterization methods need to be developed as the current methods available are not sufficient. In this thesis, the theoretical background behind wetting phenomena on hydrophobic surfaces and various techniques for characterizing wetting properties are presented. Furthermore, a new characterization technique applied to hollow, non planar surfaces and more specifically to transparent tubes is proposed. This technique measures wetting inhomogeneities using magnetically controlled water-like droplets over the entire length of the samples. This technique can measure the retentive force, a dissipative force related to the contact angle hysteresis at the three-phase contact line. This technique is used to see differences in wetting properties using reference tubes and their annealed counterparts using two different ferrofluids. As a non-destructive and quantitative characterization method, this technique could readily be used for quality control in academia and industries.

Bibliography

[1] T. Liu and C.-J. Kim, "Turning a surface superrepellent even to completely wetting liquids", *Science*, vol. 346, no. 6213, pp. 1096–1100, 2014, ISSN: 0036-8075. DOI: 10.1126/science.1254787. eprint: https://science.sciencemag.org/content/346/6213/1096.full.pdf. [Online]. Available: https://science.sciencemag.org/content/346/6213/1096.

[2] Y. Lu, S. Sathasivam, J. Song, C. R. Crick, C. J. Carmalt, and I. P. Parkin, "Robust self-cleaning surfaces that function when exposed to either air or oil", *Science*, vol. 347, no. 6226, pp. 1132–1135, 2015, ISSN: 0036-8075. DOI: 10.1126/science.aaa0946. eprint: https://science.sciencemag.org/content/347/6226/1132.full.pdf. [Online]. Available: https://science.sciencemag.org/content/347/6226/1132.

[3] S. Liu, X. Liu, S. S. Latthe, L. Gao, S. An, S. S. Yoon, B. Liu, and R. Xing, "Self-cleaning transparent superhydrophobic coatings through simple sol–gel processing of fluoroalkylsilane", *Applied Surface Science*, vol. 351, pp. 897–903, 2015, ISSN: 0169-4332. DOI: https://doi.org/10.1016/j.apsusc.2015.06.016. [Online]. Available: http://www.sciencedirect.com/science/article/pii/S0169433215013495.

[4] W. Barthlott and C. Neinhuis, "Purity of the sacred lotus, or escape from contamination in biological surfaces", *Planta*, vol. 202, pp. 1–8, Jan. 1997. DOI: 10.1007/s004250050096.

[5] L. Wang, Q. Gong, S. Zhan, L. Jiang, and Y. Zheng, "Robust anti-icing performance of a flexible superhydrophobic surface", *Advanced Materials*, vol. 28, no. 35, pp. 7729–7735, 2016. DOI: 10.1002/adma.201602480. eprint: https://onlinelibrary.wiley.com/doi/pdf/10.1002/adma.201602480. [Online]. Available: https://onlinelibrary.wiley.com/doi/abs/10.1002/adma.201602480.

[6] Y. Liu, M. Andrew, J. Li, J. Yeomans, and Z. Wang, "Symmetry-breaking in drop bouncing on curved surfaces", *Nature Communications*, vol. 6, Oct. 2015. DOI: 10.1038/ncomms10034.

[7] T. Schutzius, S. Jung, T. Maitra, G. Graeber, M. Köhme, and D. Poulikakos, "Spontaneous droplet trampolining on rigid superhydrophobic surfaces", *Nature*, vol. 527, pp. 82–85, Nov. 2015. DOI: 10.1038/nature15738.

[8] C. Guo, D. Zhao, Y. Sun, M. Wang, and Y. Liu, "Droplet impact on anisotropic superhydrophobic surfaces", *Langmuir*, vol. 34, Feb. 2018. DOI: 10.1021/acs.langmuir.7b03752.

[9] Y. Liu, L. Moevius, X. Xu, T. Qian, J. Yeomans, and Z. Wang, "Pancake bouncing on superhydrophobic surfaces", *Nature Physics*, vol. 10, Jun. 2014. DOI: 10.1038/nphys2980.

[10] L. Cao, A. K Jones, V. K Sikka, J. Wu, and D. Gao, "Anti-icing superhydrophobic coatings", *Langmuir : the ACS journal of surfaces and colloids*, vol. 25, pp. 12 444–8, Oct. 2009. DOI: 10.1021/la902882b.

[11] X. Gao, X. Yan, X. Yao, L. Xu, K. Zhang, J. Zhang, B. Yang, and L. Jiang, "The dry-style antifogging properties of mosquito compound eyes and artificial analogues prepared by soft lithography", *Advanced Materials*, vol. 19, pp. 2213–2217, Sep. 2007. DOI: 10.1002/adma.200601946.

[12] J. Li, X. Zhou, J. Li, L. Che, J. Yao, G. McHale, M. K. Chaudhury, and Z. Wang, "Topological liquid diode", *Science Advances*, vol. 3, no. 10, 2017. DOI: 10.1126/sciadv.aao3530. eprint: https://advances.sciencemag.org/content/3/10/eaao3530.full.pdf. [Online]. Available: https://advances.sciencemag.org/content/3/10/eaao3530.

[13] N. Li, L. Wu, C. Yu, H. Dai, T. Wang, Z. Dong, and L. Jiang, "Ballistic jumping drops on superhydrophobic surfaces via electrostatic manipulation", *Advanced Materials*, vol. 30, no. 8, p. 1 703 838, 2018. DOI: 10.1002/adma.201703838. eprint: https://onlinelibrary.wiley.com/doi/pdf/10.1002/adma.201703838. [Online]. Available: https://onlinelibrary.wiley.com/doi/abs/10.1002/adma.201703838.

[14] H. Dong, M. Cheng, Y. Zhang, H. Wei, and F. Shi, "Extraordinary drag-reducing effect of a superhydrophobic coating on a macroscopic model ship at high speed", *J. Mater. Chem. A*, vol. 1, pp. 5886–5891, Apr. 2013. DOI: 10.1039/C3TA10225D.

[15] R. J. Daniello, N. E. Waterhouse, and J. Rothstein, "Drag reduction in turbulent flows over superhydrophobic surfaces", *Physics of Fluids*, vol. 21, Aug. 2009. DOI: 10.1063/1.3207885.

[16] Y. Hou, M. Yu, X. Chen, Z. Wang, and S. Yao, "Recurrent filmwise and dropwise condensation on a beetle mimetic surface", *ACS nano*, vol. 9, Dec. 2014. DOI: 10.1021/nn505716b.

[17] H. Zhu, R. Duan, X. Wang, J. Yang, J. Wang, Y. Huang, and F. Xia, "Prewetting dichloromethane induced aqueous solution adhered on cassie superhydrophobic substrates to fabricate efficient fog-harvesting materials inspired by namib desert beetles and mussels", *Nanoscale*, vol. 10, pp. 13 045–13 054, 27 2018. DOI: 10.1039/C8NR03277G. [Online]. Available: http://dx.doi.org/10.1039/C8NR03277G.

[18] Y. Liu, Y. Song, H.-B. Jiang, S. Li, C. Kaya, T. Stegmaier, Z. Han, and L. Ren, "A bioinspired structured graphene surface with tunable-wetting and high wearable property for efficient fog collection", *Nanoscale*, vol. 10, Jul. 2018. DOI: 10.1039/C8NR04109A.

[19] J. Zimmermann, F. A. Reifler, G. Fortunato, L.-C. Gerhardt, and S. Seeger, "A simple, one-step approach to durable and robust superhydrophobic textiles", *Advanced Functional Materials*, vol. 18, pp. 3662–3669, Nov. 2008. DOI: 10.1002/adfm.200800755.

[20] T. S. Wong, T. Sun, L. Feng, and J. Aizenberg, "Interfacial materials with special wettability", *MRS Bulletin*, vol. 38, May 2013. DOI: 10.1557/mrs.2013.99.

[21] D. Quéré, "Non-sticking drops", *Reports on Progress in Physics*, vol. 68, p. 2495, Sep. 2005. DOI: 10.1088/0034-4885/68/11/R01.

[22] A. Ajdari and L. Bocquet, "Giant amplification of interfacially driven transport by hydrodynamic slip: Diffusio-osmosis and beyond", *Physical review letters*, vol. 96, p. 186 102, Jun. 2006. DOI: 10.1103/PhysRevLett.96.186102.

[23] C. Cottin-Bizonne, J.-L. Barrat, L. Bocquet, and E. Charlaix, "Low friction flows of liquids at nanopatterned interfaces", *Nature materials*, vol. 2, pp. 237–40, May 2003. DOI: 10.1038/nmat857.

[24] A. Egatz-Gomez, S. Melle, A. A. García, S. A. Lindsay, M. Márquez, P. Domínguez García, M. Rubio, S. T. Picraux, J. L. Taraci, T. Clement, D. Yang, M. A. Hayes, and D. Gust, "Discrete magnetic microfluidics", *Applied Physics Letters*, vol. 89, p. 034 106, Jul. 2006. DOI: 10.1063/1.2227517.

[25] H. Mertaniemi, R. Forchheimer, O. Ikkala, and R. H. A. Ras, "Rebounding droplet-droplet collisions on superhydrophobic surfaces: From the phenomenon to droplet logic", *Advanced Materials*, vol. 24, no. 42, pp. 5738–5743, 2012. DOI: 10.1002/adma.201202980. eprint: https://onlinelibrary.wiley.com/doi/pdf/10.1002/adma.201202980. [Online]. Available: https://onlinelibrary.wiley.com/doi/abs/10.1002/adma.201202980.

[26] S. Beckford, N. Langston, M. Zou, and R. Wei, "Fabrication of durable hydrophobic surfaces through surface texturing", *Applied Surface Science*, vol. 257, no. 13, pp. 5688–5693, 2011, ISSN: 0169-4332. DOI: https://doi.org/10.1016/j.apsusc.2011.01.074. [Online]. Available: http://www.sciencedirect.com/science/article/pii/S0169433211001103.

[27] V. Liimatainen, M. Vuckovac, V. Jokinen, V. Sariola, M. Hokkanen, Q. Zhou, and R. Ras, "Mapping microscale wetting variations on biological and synthetic water-repellent surfaces", *Nature Communications*, vol. 8, no. 1, Dec. 2017, ISSN: 2041-1723. DOI: 10.1038/s41467-017-01510-7.

[28] J. V I Timonen, M. Latikka, O. Ikkala, and R. Ras, "Free-decay and resonant methods for investigating the fundamental limit of superhydrophobicity", *Nature communications*, vol. 4, p. 2398, Sep. 2013. DOI: 10.1038/ncomms3398.

[29] J. Zheng, K. Yu, J. Zhang, J. Wang, and C. Li, "Modeling of the propulsion hydrodynamics for the water strider locomotion on water surface", *Procedia Engineering*, vol. 126, pp. 280–284, 2015, ISSN: 1877-7058. DOI: https://doi.org/10.1016/j.proeng.2015.11.242. [Online]. Available: http://www.sciencedirect.com/science/article/pii/S1877705815035717.

[30] B. S. Prabhupada, "Bhagavad-gita as it is", *Bhaktivedanta Book Trust*, 1983.

[31] T. Young, "Iii. an essay on the cohesion of fluids", *Philosophical Transactions of the Royal Society of London*, vol. 95, pp. 65–87, 1805. DOI: 10.1098/rstl.1805.0005. eprint: https://royalsocietypublishing.org/doi/pdf/10.1098/rstl.1805.0005. [Online]. Available: https://royalsocietypublishing.org/doi/abs/10.1098/rstl.1805.0005.

[32] A. Marmur, C. Della Volpe, S. Siboni, A. Amirfazli, and J. W. Drelich, "Contact angles and wettability: Towards common and accurate terminology", *Surface Innovations*, vol. 5, no. 1, pp. 3–8, 2017. DOI: 10.1680/jsuin.17.00002. eprint: https://doi.org/10.1680/jsuin.17.00002. [Online]. Available: https://doi.org/10.1680/jsuin.17.00002.

[33] A. Marmur and B. Krasovitski, "Line tension on curved surfaces: Liquid drops on solid micro- and nanospheres", *Langmuir*, vol. 18, pp. 8919–8923, Nov. 2002. DOI: 10.1021/la026167i.

[34] R. N. Wenzel, "Resistance of solid surfaces to wetting by water", *Industrial & Engineering Chemistry*, vol. 28, no. 8, pp. 988–994, 1936. DOI: 10.1021/ie50320a024.

[35] B. Bhushan and E. K. Her, "Fabrication of superhydrophobic surfaces with high and low adhesion inspired from rose petal", *Langmuir*, vol. 26, no. 11, pp. 8207–8217, 2010, PMID: 20131881. DOI: 10.1021/la904585j. eprint: https://doi.org/10.1021/la904585j. [Online]. Available: https://doi.org/10.1021/la904585j.

[36] M. Reyssat, J. Yeomans, and D. Quéré, "Impalement of fakir drops", *Europhysics Letters*, vol. 81, p. 26 006, Dec. 2007. DOI: 10.1209/0295-5075/81/26006.

[37] Wikipedia, *Fakir on bed of nails, benares india*, https://fi.wikipedia.org/wiki/Tiedosto:Fakir_on_bed_of_nails_Benares_India_1907.jpg, Accessed on 31-07-19, 1907.

[38] A. B. D. Cassie and S. Baxter, "Wettability of porous surfaces", *Trans. Faraday Soc.*, vol. 40, pp. 546–551, 0 1944. DOI: 10.1039/TF9444000546. [Online]. Available: http://dx.doi.org/10.1039/TF9444000546.

[39] T. Nishino, M. Meguro, K. Nakamae, M. Matsushita, and Y. Ueda, "The lowest surface free energy based on cf3 alignment", *Langmuir*, vol. 15, no. 13, pp. 4321–4323, 1999. DOI: 10.1021/la981727s. eprint: https://doi.org/10.1021/la981727s. [Online]. Available: https://doi.org/10.1021/la981727s.

[40] T. Huhtamäki, X. Tian, J. Korhonen, and R. Ras, "Surface-wetting characterization using contact-angle measurements", *Nature Protocols*, vol. 13, Jul. 2018. DOI: 10.1038/s41596-018-0003-z.

[41] C. J. R. Vicor M. Starov Manuel G. Velarde, *Wetting and Spreading Dynamics*. Taylor and Francis Group, 2007, pp. 27–28. DOI: https://doi.org/10.1201/9781420016178.

[42] K. Liu, M. Vuckovac, M. Latikka, T. Huhtamäki, and R. H. A. Ras, "Improving surface-wetting characterization", *Science*, vol. 363, no. 6432, pp. 1147–1148, 2019, ISSN: 0036-8075. DOI: 10.1126/science.aav5388. eprint: https://science.sciencemag.org/content/363/6432/1147.full.pdf. [Online]. Available: https://science.sciencemag.org/content/363/6432/1147.

[43] E. Vogler, "Practical use of concentration-dependent contact angles as a measure of solid-liquid adsorption. 1. theoretical aspects", *Langmuir*, vol. 8, no. 8, pp. 2005–2012, Aug. 1992, ISSN: 0743-7463.

[44] A. Krishnan, Y.-H. Liu, P. Cha, R. Woodward, D. Allara, and E. A Vogler, "An evaluation of methods for contact angle measurement", *Colloids and surfaces. B, Biointerfaces*, vol. 43, pp. 95–8, Jul. 2005. DOI: 10.1016/j.colsurfb.2005.04.003.

[45] B. Samuel, H. Zhao, and K.-Y. Law, "Study of wetting and adhesion interactions between water and various polymer and superhydrophobic surfaces", *The Journal of Physical Chemistry C*, vol. 115, no. 30, pp. 14 852–14 861, 2011. DOI: 10.1021/jp2032466. eprint: https://doi.org/10.1021/jp2032466. [Online]. Available: https://doi.org/10.1021/jp2032466.

[46] D. Richard and D. Quéré, "Viscous drops rolling on a tilted non-wettable solid", *Europhysics Letters*, vol. 48, no. 3, pp. 286–291, Nov. 1999. DOI: 10.1209/epl/i1999-00479-1. [Online]. Available: https://doi.org/10.1209%2Fepl%2Fi1999-00479-1.

[47] P. Hao, C. Lv, Z. Yao, and F. He, "Sliding behavior of water droplet on superhydrophobic surface", *Europhysics Letters*, vol. 90, no. 6, p. 66 003, Jun. 2010. DOI: 10.1209/0295-5075/90/66003. [Online]. Available: https://doi.org/10.1209%2F0295-5075%2F90%2F66003.

[48] M. Reyssat, D. Richard, C. Clanet, and D. Quéré, "Dynamical superhydrophobicity", *Faraday Discuss.*, vol. 146, pp. 19–33, 0 2010. DOI: 10.1039/C000410N. [Online]. Available: http://dx.doi.org/10.1039/C000410N.

[49] A. Ricchiuto and A. Tozzi, "Motion of a harmonic oscillator with sliding and viscous friction", *American Journal of Physics*, vol. 50, pp. 176–179, Feb. 1982. DOI: 10.1119/1.12881.

[50] C. Extrand and S. I. Moon, "Measuring contact angles inside of capillary tubes with a tensiometer", *Journal of Colloid and Interface Science*, vol. 431, pp. 200–203, 2014, ISSN: 0021-9797. DOI: https://doi.org/10.1016/j.jcis.2014.06.032. [Online]. Available: http://www.sciencedirect.com/science/article/pii/S0021979714004512.

[51] C. Extrand, "Forces, pressures and energies associated with liquid rising in nonuniform capillary tubes", *Journal of Colloid and Interface Science*, vol. 450, pp. 135–140, 2015, ISSN: 0021-9797. DOI: https://doi.org/10.1016/j.jcis.2015.03.007. [Online]. Available: http://www.sciencedirect.com/science/article/pii/S0021979715002581.

[52] N. Gao, F. Geyer, D. W. Pilat, S. Wooh, v. doris vollmer, H.-J. Butt, and R. Berger, "How drops start sliding over solid surfaces", *Nature Physics*, vol. 14, Feb. 2018. DOI: 10.1038/nphys4305.

[53] C. Extrand and A. Gent, "Retention of liquid drops by solid surfaces", *Journal of Colloid and Interface Science*, vol. 138, no. 2, pp. 431–442, 1990, ISSN: 0021-9797. DOI: https://doi.org/10.1016/0021-9797(90)90225-D. [Online]. Available: http://www.sciencedirect.com/science/article/pii/002197979090225D.

[54] A. ElSherbini and A. Jacobi, "Retention forces and contact angles for critical liquid drops on non-horizontal surfaces", *Journal of Colloid and Interface Science*, vol. 299, no. 2, pp. 841–849, 2006, ISSN: 0021-9797. DOI: https://doi.org/10.1016/j.jcis.2006.02.018. [Online]. Available: http://www.sciencedirect.com/science/article/pii/S0021979706001202.

[55] E. B. Dussan V., "On the ability of drops to stick to surfaces of solids. part 3. the influences of the motion of the surrounding fluid on dislodging drops", *Journal of Fluid Mechanics*, vol. 174, pp. 381–397, 1987. DOI: 10.1017/S002211208700017X.

[56] R. Massart, "Preparation of aqueous magnetic liquids in alkaline and acidic media", *IEEE Transactions on Magnetics*, vol. 17, no. 2, pp. 1247–1248, Mar. 1981, ISSN: 0018-9464. DOI: 10.1109/TMAG.1981.1061188.

[57] C. W. Extrand and Y. Kumagai, "Liquid drops on an inclined plane: The relation between contact angles, drop shape, and retentive force", *Journal of Colloid and Interface Science*, vol. 170, no. 2, pp. 515–521, 1995, ISSN: 0021-9797. DOI: https://doi.org/10.1006/jcis.1995.1130. [Online]. Available: http://www.sciencedirect.com/science/article/pii/S0021979785711307.

[58] D. W. Pilat, P. Papadopoulos, D. Schäffel, D. Vollmer, R. Berger, and H.-J. Butt, "Dynamic measurement of the force required to move a liquid drop on a solid surface", *Langmuir*, vol. 28, no. 49, pp. 16 812–16 820, 2012, PMID: 23181385. DOI: 10.1021/la3041067. eprint: https://doi.org/10.1021/la3041067. [Online]. Available: https://doi.org/10.1021/la3041067.